Therapeutic Application of α-Klotho in Peripheral Nerve Injury and Optical Atrophy

Ylenia Pérez Paredes

Master's in Biochemistry, Molecular Biology, and Biomedicine

Group of Gene Therapy for Neurometabolic Disorders

Department of Biochemistry and Molecular Biology, UAB

Directed by: Dr. Assumpció Bosch Merino

Co-supervised by: Dr. Sergi Verdés Franquesa and Rubén Guerrero Yagüe

Barcelona, 2025

Statement of publication rights

This thesis, submitted by master's candidate Ylenia Pérez Paredes, describes research carried out in my laboratory at the Institut de Neurociècies, at the Universitat Autònoma de Barcelona (UAB). All the information and results contained herein are presented with my consent. The thesis is submitted with the sole aim of evaluating the work done by the master's candidate. We do not authorize it to be published by the UAB library, as it contains preliminary results leading to a future peer reviewed publication.

Dr. Assumpció Bosch Merino
Master's project supervisor
Dept. of Biochemistry and Molecular Biology, UAB

ABSTRACT

Injuries affecting peripheral or central nerves often lead to major deficits in motor and sensory function, underscoring their profound impact on patients' lives. Existing therapeutic strategies include non-surgical approaches, pharmacological approaches, administration of growth factors, and surgical interventions. However, these strategies still fail to address the complex regeneration environment in the Peripheral and Central Nervous Systems (PNS and CNS), and no effective approach is available for nervous injuries affecting both systems.

Thus, gene therapy is a promising approach due to its cell-type specificity, ability to provide long-term effects without constant readministration, and less invasive surgeries. In this context, the anti-aging protein α-Klotho presents as a strong candidate given its multifaceted effects on neuroinflammation, oxidative stress, apoptosis, and myelination, processes central to nerve regeneration. This work has aimed to evaluate the effect of α-Klotho in degeneration, regeneration, and remyelination in the PNS, and, on the other hand, to test an engineered AAV2 capsid for future application in optic nerve degeneration.

Here, we have analyzed endogenous α-Klotho expression at the mRNA level after sciatic nerve resection and crush as distinct models for peripheral nerve injury (PNI), highlighting temporal and tissue-dependent differential regulation. *In vitro*, evaluating AAV-mediated sKL overexpression, we have detected a significant promotion in neuritogenesis in rat DRG organotypic cultures. *In vivo*, sKL overexpression through gene therapy with intrathecal administration enhanced axonal regeneration and remyelination in the tibial nerve after sciatic nerve cut-and-paste. With a view to its application in optic nerve atrophy, we have assessed the tropism of an engineered AAV2.GL capsid with different promoters, finding that under the control of the CAG promoter, higher retinal neuronal tropism was achieved than with the CMV promoter. Our results suggest that AAV-mediated α-Klotho overexpression improves nerve regeneration and remyelination, with potential clinical applications in PNI and optic nerve degeneration.

ABBREVIATIONS

AAV: Adeno-Associated Viruses
ANS: Autonomic nervous system
BBB: Blood-brain barrier
BDNF: Brain-derived neurotrophic factor
CAG: Chicken beta-actin
cDNA: Complementary DNA
CMV: Cytomegalovirus
CNS: Central Nervous System
CSF: Cerebrospinal fluid
CSPG: Chondroitin sulfate proteoglycans
DIV: Days *in vitro*
dpi: Days post-injury
DRG: Dorsal root ganglia
EDL: *Extensor digitorum longus muscle*
ELISA: Enzyme-linked immunosorbent assay
ER: Endoplasmic Reticulum
FBS: Fetal Bovine Serum
FGF23: Fibroblast growth factor 23
FOXO3a: Forkhead Box O 3a
GDNF: Glial cell-derived neurotrophic factor
GFP: Green fluorescent protein
GM: Gastrocnemius
HSPG: Heparan sulfate proteoglycans
hSyn: Human synapsin
ITRs: Inverted Terminal Repeat
KL: α-klotho protein
MAG: Myelin-associated glycoprotein
MAIs: Myelin-associated inhibitors
MAMs: mitochondria-associated membranes
MBP: *Myelin Basic Protein*
mKL: Membrane α-klotho
MPZ: *Myelin Protein Zero*
NAD+: Nicotinamide adenine dinucleotide
NBF: Neutral Buffered Formalin
NF-kB: Nuclear Factor Kappa-B
NGF: Nerve growth factor
NGS: Normal Goat Serum
NOGO: Neurite outgrowth inhibitor
NTC: Non-Template Control
P/S: Penicillin/streptomycin
PEG: Polyethylene Glycol
PGP 9.5: Protein gene product 9.5
pKL: Proteolyzed α-Klotho
PNI: Peripheral Nerve Injury
PNS: Peripheral Nervous System
PolyA: Polyadenylation
p-sKL: Proteolytically cleaved soluble α-Klotho
qPCR: Quantitative PCR
RAGs: Regeneration-associated genes
RER1: Retention in Endoplasmic Reticulum Sorting Receptor 1
RGCs: retinal ganglion cells
ROI: *Region Of Interest*
RPLP0: Ribosomal Protein Lateral Stalk Subunit P0
SC: Spinal Cord
scAAV: Self-complementary AAV
SCs: Schwann cells
sKL: Secreted soluble α-klotho
SNC: Sciatic Nerve Crush
SNI: Sciatic nerve injury
SNR: Sciatic Nerve Resection
SNS: somatic nervous system
Sol: Soleus
ssDNA: single-stranded DNA
SV40: Simian Virus 40
TA: Tibialis Anterior
Trx/Prx: Thioredoxin/peroxiredoxin
vg: Viral genomes
VP3: Viral Protein 3
WD: Wallerian degeneration
Wfs1: Wolframin ER Transmembrane Glycoprotein

INDEX OF CONTENT

INTRODUCTION

1. The nervous system

1.1. Overview of the Central and Peripheral Nervous System

The nervous system comprises a complex network of tissues responsible for processing sensory stimuli from the environment, generating motor responses, and controlling visceral functions (1). According to anatomical and functional criteria, it is divided into the Central Nervous System (CNS) and Peripheral Nervous System (PNS). CNS can be divided into the brain (brainstem, cerebellum, diencephalon, and cerebral hemispheres) and the spinal cord, while PNS consists of nerves (autonomic, spinal, and cranial) and ganglia. Although most cranial nerves are part of the PNS, the olfactory and optic nerves are CNS tracts. Both are myelinated by oligodendrocytes and wrapped around meningeal sheaths (2).

Nervous tissue includes both neurons and glial cells. Neurons are specialized cells that conduct electrochemical signals through synapses, facilitating impulse transmission. Glial cells can be broadly categorized into macroglia (oligodendrocytes, astrocytes, and oligodendrocyte precursor cells in the CNS; and Schwann and satellite cells in the PNS) and microglia. These cells have an active role in the nervous system homeostasis, as they are involved in structural, metabolic, and immune response functions (3,4).

1.2. Functional organization of the PNS and CNS

Axonal fibers in the PNS are divided into afferent (sensory) and efferent (motor). Sensory neurons bring peripheral information through ascending pathways to the spinal cord and the brain, with their cell bodies located in the dorsal root ganglia (DRG) (5). In contrast, the conduction of information in the motor neurons is from the CNS to the periphery, with their somata located in the ventral horn of the spinal cord. These motor neurons are organized into the autonomic nervous system (ANS) and the somatic nervous system (SNS). The function of the ANS is to regulate involuntary processes, whereas the SNS controls skeletal muscles and voluntary actions (5).

As a CNS tract, the optic nerve is composed of axons from retinal ganglion cells (RGCs) and carries sensory information to the brain. At the optic disc, RGC axons converge and form the optic nerve, which is myelinated as it exits the retina. The retina is organized into specific layers, from the ganglion cell layer to the photoreceptors, and is protected by the blood-retinal barrier and the internal limiting membrane (2).

1.3. Structure of peripheral and central nerves

Three layers of connective tissue form the peripheral nerves: the endoneurium, which surrounds individual axons and their Schwann cells (SCs); the perineurium, which divides the nerve into fascicles; and the epineurium, the most external layer around the entire nerve.

Meanwhile, in CNS tracts, individual axons are supported by oligodendrocytes. Rather than connective tissue layers around axonal bundles, glial cells are present, and the meninges (dura mater, arachnoid, and pia mater) surround the entire nerve (2). CNS axons' diameter and myelination are closely related to conduction velocity (6).

2. Nerve injuries

2.1. Peripheral Nerve Injury (PNI)

2.1.1. Epidemiology and clinical relevance

Peripheral nerve injury (PNI) is a significant public health concern, usually leading to major deficits in motor and sensory function. Epidemiological studies in Europe and the United States estimate the incidence of PNI to be 11.2-12.9 cases per 100.000 person-years, representing 2-3% of all trauma patients (7–9). From a socio-economic standpoint, PNI accounts for a significant burden due to the high costs of surgical interventions, rehabilitation, loss of productivity, and additional demands on healthcare systems.

2.1.2. Types and causes of PNI

PNI can be classified based on its etiology or the severity of the structural damage. PNI can occur from trauma (complete section, crushing, or stretching), compression, inflammation, or metabolic disorders such as diabetes mellitus. Depending on the severity of the damage, the Seddon and Sunderland classifications have been proposed (10,11). The Seddon system describes neuropraxia (temporal conduction block caused by an injury in the myelin sheath), axonotmesis (injury to myelin and axon requiring months for recovery), and neurotmesis (nerve transection with an incomplete recovery). The Sunderland system expanded this classification to six degrees, considering the effect on the connective tissue layers (12,13).

2.1.3. Cellular and molecular basis

Following an injury in the PNS, Wallerian degeneration (WD) occurs at the axon's distal segment within 24-48 hours post-injury. SCs, endothelial cells, macrophages, and neutrophils are key elements in WD, involved in the disruption of both axonal and myelin structures (14).

First, axonal degeneration is mediated by extracellular Ca^{2+} influx, which activates calcium-dependent proteases (calpains) that, in turn, degrade the cytoskeleton. Moreover, nicotinamide adenine dinucleotide (NAD+) levels in affected axons decrease, contributing to the degradation of the neuronal cytoskeleton. The myelin sheath also degenerates into myelin ovoids, releasing inhibitory regeneration proteins such as myelin-associated glycoprotein (MAG), which must be cleared to achieve efficient axonal regrowth. A repairing phenotype is acquired by the SCs, characterized by the downregulation of myelin-associated genes like *Myelin Protein Zero (MPZ)* and *Myelin Basic Protein (MBP)* and upregulation of trophic factors, including Glial cell-derived neurotrophic factor (GDNF), brain-derived neurotrophic factor (BDNF), and Nerve growth factor (NGF) (15).

Next, to remove axonal and myelin debris, there is macrophage recruitment mediated by pro-inflammatory cytokines (IL-1β, IL-6, TNF-α) produced by SCs. Resident macrophages are the first to infiltrate within hours post-injury, whereas circulating macrophages arrive 2-3 days later (15). SCs also phagocytose axonal and myelin debris. This results in muscle atrophy due to the loss of connectivity between the target muscle and the distal nerve stump.

2.2. Optic nerve atrophy

The progressive loss of RGCs is characteristic of optic atrophy, leading to impaired transmission of visual information. Worldwide, optic nerve atrophy is one of the primary causes of blindness and irreversible loss of vision (16), underscoring its profound impact on patients' lives.

2.2.1. Classification and etiology

Optic atrophy represents the potential outcome of serious disorders affecting the CNS that damage RGCs, making it a sign of an underlying condition, which can often be missed (17).

The main types of optic nerve atrophy are primary (caused by direct injury to the optic nerve axons), secondary (caused by severe edema), consecutive (caused by retinal or vascular diseases), and glaucomatous (17). Etiological factors encompass traumatic, compressive, post-inflammatory, ischemic, metabolic, demyelinating, and hereditary causes (17). Based on recent etiologic studies, traumatic injuries and CNS diseases are the most common etiologies (16,17).

2.2.2. Molecular and biochemical basis

In optic atrophy, RGC death is driven by oxidative stress, neuroinflammation, vascular disruption, endoplasmic reticulum (ER) stress, mitochondrial dysfunction, and axonal retrograde degeneration. Oxidative stress is one of the earliest events that, through caspase activation and cytochrome c release, induces apoptosis (18). Neuroinflammation mediated by pro-inflammatory cytokines and hypoxia due to vascular loss and metabolic changes further exacerbates RGC loss (19). The upregulation of ER stress markers and mitochondrial crosstalk with mitochondria-associated membranes (MAMs) also plays a key role (20). Likewise, mitochondrial dysfunction and cytoskeletal disruption participate in axonal degeneration (19,21). The poor capacity for remyelination in the CNS, largely due to the presence of myelin-associated inhibitors (MAIs), results in ongoing RGC loss (22).

2.3. Regeneration in the PNS and CNS

In nerve injury, regeneration relies on remyelination, axonal re-growth from newly emerging sprouts, and a regulated neuroinflammatory environment.

2.3.1. PNS regeneration mechanisms

Following WD after a PNI, functional regeneration is possible thanks to the crucial role of SCs, which create a suitable supportive environment around the site of the injury (23). In this environment, myelin debris is efficiently phagocytosed by macrophages and SCs, preventing scar formation (24). The PNS regeneration process continues with the regenerative bridge, composed of extracellular matrix and inflammatory cells, serving as an axonal guide capable of fusing the distal and proximal nerve stumps. Also, bands of Büngner formed by SCs facilitate the orientation of axons. Moreover, signalling molecules translated by ribosomes in PNS axons aid in the new growth cone development (25). Gene expression changes are also present in nerve regeneration, with an upregulation of regeneration-associated genes (RAGs). RAG expression is regulated by histone acetylation at RAG promoters (25), an epigenetic modification that tends to increase after PNI.

Despite the regenerative capacity of the PNS, unresolved Wallerian degeneration could result in a persistent inflammatory response, altered secretion of neurotrophic factors, and ineffective revascularization, among other issues. Complete functional recovery is not always possible after serious injuries with poor axonal orientation or chronic denervation of the target muscles (26).

2.3.2. CNS regeneration mechanisms

In the CNS, nerve regeneration is less effective compared to the PNS. This is not due to a lower intrinsic neuronal capacity for regeneration in the CNS, since it has been proven that these neurons could grow within a PNS environment (27). Instead, regeneration in the CNS is primarily limited by environmental barriers.

Oligodendrocytes represent the biggest limitation because they do not provide the required biochemical environment. This molecular inhibition is linked with an inhibitory protein profile mediated by pro-inflammatory cytokines, chondroitin sulfate proteoglycans (CSPG), and MAIs, for instance, MAG or Neurite outgrowth inhibitor (NOGO) (25). In addition, neurotrophic factors are drastically reduced. Reactive astrocytes and microglia, forming the glial scar, further alter the phagocytosis of myelin debris after a CNS injury (24). Structural barriers also arise, as the injury becomes trabecular-like and axonal sprouting remains minimal, resulting in poor microtubule stabilization in axonal growth cones (25). Finally, intrinsic limitations, including the lack of ribosomes and mRNA and insufficient upregulation of RAGs, further restrict CNS regeneration (25).

3. Experimental models of nerve injury

3.1. In vitro models

The use of cell lines offers ethical advantages by aligning with the 3Rs principles and enhancing translational research, especially when derived from human tissues. However, the main limitation is the lack of complex cellular interactions, which limits their ability to accurately predict the *in vivo* response to nerve injury (15).

To overcome this problem, organotypic cultures reproduce the three-dimensional tissue architecture while preserving physiological cellular interactions. DRG organotypic cultures are relevant in nerve regeneration research, with neurite outgrowth usually being analyzed. Despite these advantages, these models present several drawbacks, including their short survival time, the lack of integration within the whole animal organism, and the variability of endogenous axotomy introduced during explant generation (15).

3.2. In vivo models

3.2.1. PNI models

Animal models are widely used in nerve injury research, with rodents being the most used due to their solid nerve regeneration, resistance to infections after surgeries, availability, and cost (28). Among peripheral nerves, the sciatic nerve is the preferred nerve for experimental studies. Sciatic nerve injury models offer several benefits: they are extensively described in the literature, supported by a range of functional and behavioural tests, and involve the major mixed peripheral nerve (28).

Several injury methods can be applied to the sciatic nerve (29). Compression injuries, also known as crush injuries, damage the axon and myelin structures without affecting the connective tissue (axonotmesis). Transection or resection injuries closely replicate severe nerve injuries in humans, as complete sciatic nerve transection without surgical reconstitution models chronic denervation. In contrast, techniques like direct suture repair or "cut-and-paste" using fibrin glue (30) secure the two nerve segments together after the injury. Within these models, axonal and myelin regeneration can be evaluated with histology and morphometry, as well as functional tests including electrophysiology and *in vivo* imaging (12).

3.2.2. Optic nerve atrophy models

Among the various models used to study optic nerve atrophy, our research group works with Wfs1 mutant rats (Plaas et al., 2017), which are generated by a deletion in the *Wfs1* gene. These animals are models of Wolfram Syndrome (WS), a rare neurodegenerative disease. At 3 months old, Wfs1 knockout animals start developing cataracts, followed by the degeneration of RGCs, finally leading to bilateral optic atrophy and blindness at 15 months (31).

4. Available therapeutic strategies for nerve injury

With the current therapeutic strategies, a complete functional recovery after severe nerve injury in either the PNS or CNS is not achievable. However, non-surgical approaches such as aerobic physical exercise, electrostimulation, low-intensity ultrasound, and phototherapy have shown positive effects on the synthesis of growth and neurotrophic factors (12). Surgical interventions are common in clinical practice, with autograft as the gold standard in critical nerve injuries (15). Pharmacological strategies (steroid hormones, corticosteroids, B vitamins, antioxidant therapies, etc.) aim to reduce inflammation, oxidative stress, and metabolic stress (12). Growth factor administration (NGF, BDNF, or GDNF) also helps with regeneration. Overall, the duality of the regeneration environment in the PNS and the CNS underscores the need for therapeutic strategies that work in both contexts.

5. Klotho

Klotho is considered an anti-aging gene that encodes the α-klotho protein (KL). Interestingly, the name originates from the Greek goddess Klotho, who is believed to determine the beginning of human life (32). It was first discovered by Kuro-O et al. (33) when they generated KL knockout mice, in which a single insertion mutation disrupted the gene and led to several human aging characteristics, including a reduced lifespan, osteoporosis, cognitive decline, hypertension, and arteriosclerosis. Accordingly, subsequent studies have shown that KL levels decrease with normal aging, neurodegenerative diseases, diabetes, and renal failure (34,35). In contrast, overexpression of KL has been shown to improve survival (35,36), cognition (37), muscle regeneration (38), and bone microstructure (39), among other conditions related to aging. These findings highlight the role of Klotho as a promising therapeutic candidate for nerve injuries.

5.1. Klotho gene, protein, and tissue expression patterns

The human Klotho gene is located on chromosome 13 (13q13.1) and is highly conserved across species. With 5 exons and 4 introns, it has 2 mRNA splice variants. The first transcript is the membrane form (mKL), which encodes a transmembrane protein and includes two domains (KL1 and KL2), a transmembrane segment, and a cytoplasmic tail. mKL functions as an obligate co-receptor of fibroblast growth factor 23 (FGF23) together with FGFR1c (40). mKL participates in mineral metabolism by modulating phosphate concentration through the ERK1/MAPK pathway and Ca^{2+} concentration by regulating ion channels and PTH production (35,41). α-secretases (mainly ADAM10 and ADAM17) can cleave KL1 or KL2 extracellular domains, releasing proteolytically cleaved soluble Klotho (p-sKL), which can consist of either the KL1 and KL2 domains separately or together. The second transcript is the secreted soluble Klotho (sKL), which includes the KL1 domain and a secretion signal (34,35). Soluble forms of Klotho have systemic effects through interactions that remain poorly described, although lipid raft interactions have been proposed to modify membrane properties (41). Thus, Klotho can be found in the extracellular space and detected in serum and cerebrospinal fluid (CSF) in two forms: either cleaved from the membrane transcript (pKL, pKL1, or pKL2) or directly derived from the shorter secreted transcript (sKL).

The KL1 and KL2 domains show similarities with the glycosidase family 1 protein and appear to have limited glycosidase capacity (40). The Klotho family includes three proteins (α, β, and γ). The expression of α-Klotho is tissue-specific, being especially high in the kidneys (renal tubules are the primary source of soluble Klotho) and the brain, particularly in the choroid plexus and CSF. It is expressed to a lesser extent in tissues such as blood vessels, skeletal muscle, pancreatic β-cells, and bladder (35,42). In human ocular tissues (specifically in the optic nerve, the retina, and the lens), α- and γ-Klotho are expressed, while the β isoform is expressed strictly in the optic nerve and the retina (43). This organ-specific expression is partly regulated by promoter methylation since the Klotho promoter is prone to methylation due to the presence of several CpG islands (44).

5.2. Klotho mechanisms of action and signaling

Klotho has a pleiotropic nature, reducing neuroinflammation, oxidative stress, excitotoxicity, ischemia, fibrosis, apoptosis, and senescence while contributing to mineral metabolism, enhancing myelination, and preserving muscle function (Fig. 1).

5.2.1. Inhibition of neuroinflammation

Klotho has a protective capacity against neuroinflammation through various mechanisms. It regulates inflammation in the CNS by inhibiting the NF-κB signaling pathway, thereby reducing pro-inflammatory cytokines, chemokines, and immune ligands (35). In addition, Klotho also inhibits the formation of the NLRP3 inflammasome to reduce production of pro-inflammatory cytokines. Moreover, this anti-inflammatory capacity of Klotho promotes macrophage and microglia polarization towards an anti-inflammatory phenotype (45).

5.2.2. Inhibition of oxidative stress and excitotoxicity

To confer resistance to oxidative stress and glutamate toxicity, Klotho activates the thioredoxin/peroxiredoxin (Trx/Prx) antioxidant system through the PI3K/Akt pathway, which ultimately phosphorylates the transcription factor Forkhead Box O 3a (FOXO3a) (35). This transcription factor controls the expression of factors related to oxidative stress resistance and metabolism, among others. Klotho also activates the transcription factor Nrf2 to increase the antioxidant response by transcribing antioxidant enzymes and, in turn, enhances NF-κB inhibition (35).

5.2.3. Inhibition of apoptosis, fibrosis, and senescence

Klotho inhibits fibrosis, apoptosis, and senescence through the TGF-β and Wnt/β-catenin signaling pathways. By binding to the type II TGF-β receptor, Klotho reduces the expression of mesenchymal markers and preserves epithelial characteristics, thereby limiting fibrosis (46). Klotho also binds to Wnt ligands and inhibits β-catenin activation, which protects against apoptosis and premature senescence (35).

5.2.4. Promotion of myelination

Myelination is promoted by Klotho, as it supports the proliferation and maturation of oligodendrocytes through the activation of Akt and ERK1/2 (47). The potential of Klotho in promoting remyelination has also been demonstrated in an induced demyelination model, where transgenic animals overexpressing Klotho exhibited a significant increase in myelinated axonal density (48).

5.2.5. Muscle mass and function preservation

Klotho plays a significant role in preserving muscle mass and function by maintaining mitochondrial homeostasis in muscle progenitor cells, in addition to inhibiting fibrosis and inflammation (49). In a Klotho-deficient mouse model (KL^{-}/KL^{-}), muscle mass decline is abundant and results in muscle degeneration (50). It is also important to note that physical exercise has been shown to increase circulating Klotho levels, supporting its beneficial effects on muscle health (51).

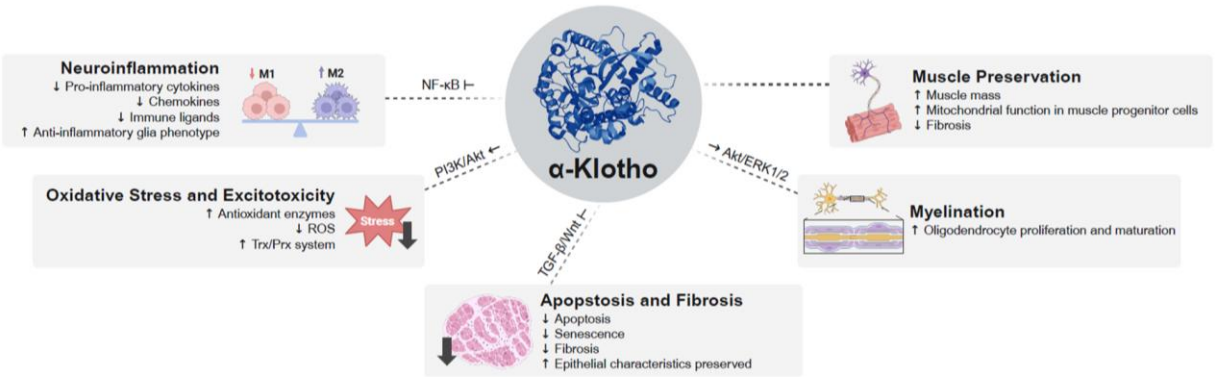

Figure 1: Klotho mechanisms of action and signaling *(Designed with Biorender).*

6. Gene therapy

6.1. Gene therapy approaches to nerve injuries

Gene therapy is a therapeutic strategy that aims to modify a defective gene through the introduction of functional nucleic acids (DNA or RNA) into target cells within the organism. Gene therapy strategies can be classified in several ways: according to the therapeutic goal (gene addition, gene correction, gene suppression, or gene interference), according to vector application (*in vivo* or *ex vivo*), and according to expression duration (transient or stable), among others. The potential of gene therapy lies in cell-type specificity, persistence over time through long-term or permanent correction of diseases lacking effective treatments, and the capacity to address the root cause of clinical disorders. Hence, gene therapy presents as a potential approach to deliver Klotho.

6.2. Overview of AAV biology and serotypes

Gene delivery vectors transport genetic material into target cells and are divided into non-viral or viral systems, with the latter being the most efficient in the nervous system. Among viral vectors, adeno-associated viruses (AAV) can package up to ~5 kb, exhibit broad capsid-dependent tropism, low immunogenicity, and mediate moderate episomal, non-integrative transduction (52).

Structurally, AAVs are non-enveloped icosahedral particles, delimited by two ITRs, that encapsulate a single-stranded DNA (ssDNA) genome. The genome comprises two open reading frames, *rep* (encoding proteins necessary for replication and transcriptional regulation) and *cap* (encoding the capsid proteins VP1, VP2, and VP3) (53). Notably, helper viruses (usually adenoviruses) are required to complete their viral life cycle. AAV transduction begins with binding to specific receptors and internalization by clathrin-mediated endocytosis, followed by intracellular trafficking, endosomal escape, and nuclear entry of the viral genome. In the nucleus, the genome is maintained episomally, and the transgene expression leads to the production of the therapeutic protein (54). To bypass the DNA synthesis of the second-strand, which is the most limiting step in transduction, self-complementary AAVs (scAAV) have been developed (54). Moreover, encapsulating dsDNA, scAAV can more easily evade cellular recognition systems for exogenous DNA.

The use of AAVs in preclinical and clinical settings is a reality, with multiple natural serotypes exhibiting differential tropism. The most relevant serotypes for this work are AAV2, with tropism for the retina (primary receptor: heparan sulfate proteoglycans, HSPG), and AAV9, with tropism for the CNS and muscle. Importantly, AAV9 binds terminal N-linked galactose, a feature that facilitates its ability to cross the blood-brain barrier (BBB) in certain conditions (53).

6.3. AAV capsid engineering

Specific tropism and efficient transduction are essential aspects in gene therapy; however, natural AAV serotypes present limitations. To overcome these, capsid engineering strategies have emerged, with methods such as directed evolution, rational design, or machine-learning-based design (55). Directed evolution creates different capsid combinations through peptide insertion, site-directed mutagenesis, or capsid shuffling, assembling them into libraries. These libraries are then screened with *in vitro*, *in vivo*, or *ex vivo* selection platforms to identify capsid candidates (55).

6.4. The AAV2.GL capsid

The novel AAV2.GL capsid was engineered by Pavlou et al. (56) using peptide insertion into the AAV2 capsid and *in vivo* selection in mice. The design aimed to increase capsid transduction efficiency in photoreceptors while using intravitreal injection as a less invasive delivery route compared to the subretinal approach, thereby reducing collateral tissue damage and improving tropism (56). Given the favourable safety profile of AAV and ongoing advances in capsid engineering, AAV2.GL represents a promising tool for optic disorders. In this study, we therefore evaluated its ability to transduce RGCs and its future application in optic atrophy.

HYPOTHESIS AND OBJECTIVES

The hypothesis of this work is that overexpression of α-Klotho enhances regeneration and remyelination following peripheral nerve injury. This project aims to evaluate the effect of α-Klotho in degeneration, regeneration, and remyelination in the PNS, and to test an engineered AAV2 capsid for future application in optic nerve degeneration. The following objectives were proposed:

1. To study endogenous α-Klotho expression at the mRNA level after sciatic nerve resection and crush as distinct models for PNI and at different timepoints.
2. To evaluate the effect of overexpressing α-Klotho on neurite outgrowth in an *in vitro* organotypic culture model of rat DRG.
3. To characterize the effect of sKL overexpression through gene therapy on axonal regeneration and remyelination in a “cut-and-paste” model of sciatic nerve injury.
4. To assess the tropism of an engineered AAV2.GL capsid combined with different promoters for retinal neurons, with a view to its application in optic nerve atrophy.

MATERIALS AND METHODS

1. DNA cloning

1.1. Generation of sKL, mKL, and null plasmid constructs

The plasmids pAAV-CMV-sKL, pAAV-CMV-mKL, and pAAV-CMV-Null used in this work for producing gene therapy viral vectors were previously generated by our research group at the Universitat Autònoma de Barcelona. These three constructs were used for the organotypic cultures; and for the sciatic nerve cut-and-paste injury model, self-complementary constructs were used (pscAAV-CMV-sKL, pscAAV-CMV-mKL, and pscAAV-CMV-Null).

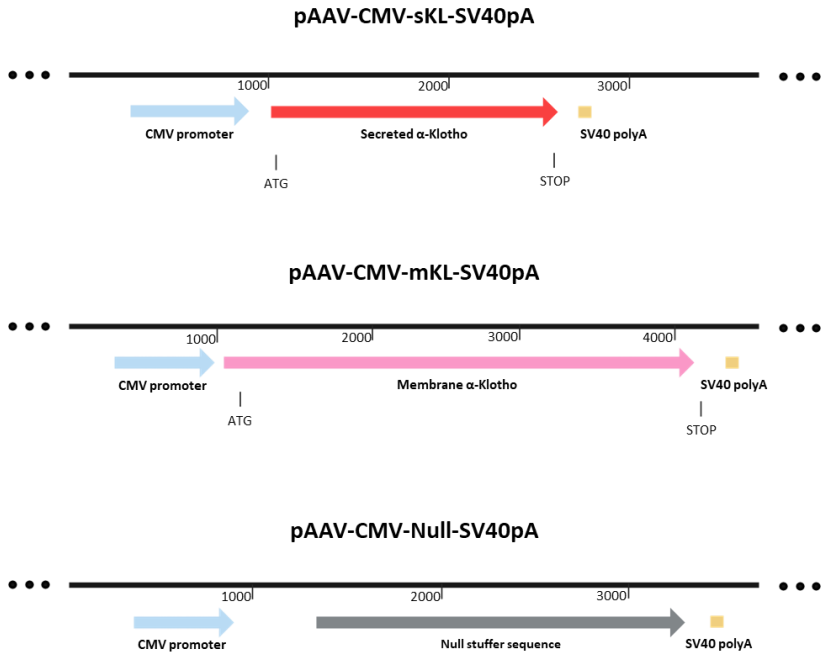

Figure 2: Constructs used in AAV vectors for organotypic DRG cultures and the sciatic nerve cut-and-paste injury model.

The pAAV-CMV-sKL and pAAV-CMV-mKL plasmids (Fig. 2) contained the mouse secreted Klotho (sKL) or membrane Klotho (mKL) sequence, respectively, under the control of the Cytomegalovirus (CMV) promoter. A Simian Virus 40 (SV40) polyadenylation (polyA) site was included at the end of the constructs. As a control, the pAAV-CMV-Null plasmid (Fig. 2) was generated with a non-coding stuffer sequence under the control of the CMV promoter.

The cloning initially consisted of the digestion of the plasmid backbone and inserts with specific restriction enzymes (ThermoFisher Scientific and NEB: New England Biolabs). Next, gel electrophoresis was used to separate the digested DNA fragments, followed by purification with a commercial kit (NucleoSpin Gel and PCR Clean-up, Machery-Nagel). To avoid self-ligation, the backbone was dephosphorylated (FASTAP, ThermoFisher), and ligation with the insert was performed (T4 ligase, NEB). Ligation products were transformed into chemically competent *Escherichia coli* cells (TOP10) using a heat-shock protocol. Finally, ampicillin-resistant colonies were selected, and the amplification of the plasmids was performed in bacterial cultures following the manufacturer's instructions using the E.Z.N.A.® Plasmid DNA Maxi Kit (Omega Bio-Tek).

1.2. Generation of pscAAV2.GL-CMV-GFP and pscAAV2.GL-CAG-GFP

Conversely, the AAV2.GL capsid variant construct used for viral tropism in retina studies was produced based on the protocol of Pavlou et al. (56), using an overlapping PCR strategy that introduced a specific insertion into the AAV2 capsid with a megaprimer-directed mutagenesis.

The insertion sequence described in this paper was RGNAAA GLSPPTR AARQ, composed of 7-mer amino acids (GLSPPTR), specifically inserted between N587 and R588 in the AAV2 wild-type capsid with alanine linkers. Therefore, we designed a synthetic megaprimer (~200 bp) with the insert in the central region (Table 1).

Table 1: Megaprimer for overlapping PCR strategy. The sequence in bold corresponds to the inserted region.

Megaprimer	Length (bp)
AGACGAAGAGGAAATCAGGACAACCAATCCCGTGGCTACGGAGCAGTATGGTTCTGTATCTACCAACCT CCAGAGAGGCAACGCCGCCGCC**GGCCTGAGCCCCCCCACCAGA**GCCGCCAGACAAGCAGCTACCG CAGATGTCAACACACAAGGCGTTCTTCCAGGCATGGTCTGGCAGGACAGAGATGTGTACCTTCAGG	201

The overlapping PCR was prepared in a final volume of 25 µL, containing 5 µL of 5x reaction buffer, 0.25 µL of high-fidelity Q5 polymerase, 0.75 µL of DMSO, 0.2 µL dNTPs, 1 µL of parental AAV2 capsid vector DNA (10 ng/µL), 8.85 µL of synthetic megaprimer, and nuclease-free water. The megaprimer was prepared to achieve a molar excess 500-fold greater than 10 ng of the AAV2 capsid plasmid (~147.6 ng). The reaction was performed in a thermocycler (GE-96G, BIOER Gene Explorer) following the program: initial denaturation at 98°C for 2 min; 25 cycles of 98°C for 30s, primer annealing at 50 °C for 1 min, and extension at 72 °C 11 min and 10 s (90 s/kb); final extension at 72 °C for 12 min.

To remove the methylated parental AAV2 capsid plasmid, the PCR product was digested with DpnI (10 U/µL) for 1 h at 37 °C. TOP10 cells were transformed, and plasmid DNA was amplified in bacterial cultures with the E.Z.N.A.® Plasmid DNA Mini Kit (Omega Bio-Tek).

For verifying the insertion sequence, plasmids were extracted from individual colonies and screened by restriction digest analysis with *BamHI* and *PdiI* combined with *XbaI*, followed by Sanger sequencing with multiple primers targeting the specific capsid region (Table 2). Verified clones were amplified with E.Z.N.A.® Plasmid DNA Maxi Kit (Omega Bio-Tek).

Table 2: Primers for Sanger sequencing of the AAV2.GL capsid region

Sanger primers	Primer sequence	Length (bp)
CapAAV2 Fwd1	GTACCACCTCAATGGCAGAGAC	22
CapAAV2 Fwd2	TAGGAACTGGCTTCCTGGAC	20
CapAAV2 Fwd3	ACCTGTATTACTTGAGCAGAAC	22
CapAAV2 Fwd4	AGCAGTATGGTTCTGTATCTACC	23

2. AAV vectors production

The AAV vectors generated for the organotypic DRG cultures, the sciatic nerve cut-and-paste injury model, and the biodistribution studies were produced at the Universitat Autònoma de Barcelona, specifically at the Unitat de Producció de Vectors (UPV) biosafety facilities.

2.1. Tri-transfection of HEK 293AAV cells and harvest

HEK 293 cells were transfected with the triple transfection method (57) in equimolar concentration for producing the AAV vectors: the plasmid pXX6, which promotes adenoviral helper genes; pRep2Cap9 for proper replication and capsid formation; and the plasmid with the transgene (sequence of interested) flanked by Inverted Terminal Repeat (ITRs), using PEI (PolyScience) as the transfection agent. After an incubation of 6 h in a standard incubator (37 °C, 95% humidity, and 5% CO2), the transfection media (1% FBS) was replaced with growth media (10% FBS). Forty-eight hours later, the cells and the supernatant were harvested and centrifuged, then stored at -80 °C and -20 °C, respectively.

2.2. AAV vector purification

To release intracellular viral particles, the cell pellets were subjected to 3 freeze/thaw cycles, centrifugation, and 50 U/mL benzonase treatment (1 h at 37 °C, Sigma) to degrade non-encapsulated DNA. Next, the viral particles were precipitated with 40% polyethylene glycol (PEG) and 200 mM NaCl, both in the cellular fraction and the supernatant, and then resuspended in AAV buffer (Tris 50mM, NaCl 20 mM, $MgCl_2 \cdot 6H_2O$ 2mM; pH at 8.5).

2.3. Iodixanol gradient and AAV quantification

The fractions were purified following an iodixanol gradient (15%, 25%, 40% and 60% with PBMSK) and ultracentrifuged in a Beckman 70Ti rotor (Beckman Coulter) at 69.000 rpm, for 90 minutes at 18 °C. The density band corresponding to AAV was recovered and quantified using the Quant-iT PicoGreen (ThermoFisher Scientific) method (57), which intercalates into double-stranded DNA and generates a proportional fluorescence signal that was measured in a Spark plate fluorimeter (Tecan). Detergent lysed and non-lysed AAV samples were compared to compensate for the background and contaminants, and the viral genome concentration (vg/mL) was calculated using the DNA standard curve and the AAV genome size, using a correction factor for strand hybridization.

3. Rat dorsal root ganglion (DRG) organotypic culture

Five-day-old rat pups were euthanized, and DRGs were aseptically isolated and cultured *in vitro* on a 3D collagen matrix, previously set in a 24-well plate precoated with poly-L-lysine and 600 µL of culture medium. Neurobasal™ Medium (Gibco) was supplemented with B27 (Gibco), 30% glucose, L-glutamine, and penicillin and streptomycin (P/S). Importantly, no neurotrophic factors were added.

The different experimental conditions included non-treated as a control, DRGs treated with recombinant sKL protein (100 ng/mL), and DRGs transduced with pAAV9-CMV-mKL or with pAAV9-CMV-sKL. The AAV dose was adjusted to achieve an efficient DRG infection, following previous references (≃50.000 viral genomes per cell). The organotypic cultures were maintained and periodically washed with PBS to remove the remnants of the DRG capsules for 9 days in vitro (DIV).

4. Mouse surgical procedures

4.1. Sciatic nerve injury models

4.1.1. Sciatic nerve crush (SNC)

C57BL/6J mice 2-3 months (n = 5 in the experimental group: 3 males and 2 females, and n = 7 in the sham group: 3 males and 4 females) were used for the sciatic nerve crush (SNC) model. The crush was made following the protocol by Bauder & Ferguson (58), with a forceps at 45 mm from the tip of the fourth toe for 10-20 s. The animals were euthanized (1, 3, 7, 14, or 28 days post-injury, dpi) to evaluate the endogenous sKL and mKL levels after SNC. The tissues extracted were both contralateral and ipsilateral from the sciatic nerve (proximal and distal regions), DRGs, lumbar spinal cord (from L2 to S1), gastrocnemius (GM), and soleus (Sol).

4.1.2. Sciatic nerve resection (SNR)

The injury consisted of the complete section of the sciatic nerve at 45 mm from the tip of the fourth toe, deliberately separating the nerve ends to prevent spontaneous reinnervation. C57BL/6J mice (7-7.5 months) were sacrificed at 7 or 28 dpi: at 7 dpi, 8 animals were included per group (injured or sham; sex-balanced), and at 28 dpi, 8 animals were injured and 7 were sham (4 females, 3 males). The extensor digitorum longus muscle (EDL), spinal cord (SC), tibialis anterior (TA), gastrocnemius (GM), and Soleus (Sol) were harvested with the objective to evaluate the endogenous expression of sKL and mKL in these tissues after the resection.

4.1.3. Sciatic nerve cut-and-paste

The sciatic nerve cut-and-paste injury consisted of the section of the sciatic nerve at 45 mm from the tip of the fourth toe and fibrin glue (fibronectin, fibrinogen, and thrombin) was immediately applied between both ends to join them together. Just after the injury, the viral vectors were administered via intrathecal (L3 to L4) for therapeutic purposes: scAAV9-CMV-sKL for the experimental group and scAAV9-CMV-Null as control or mock group, both at a dose of 1.5×10^{11} viral genomes in 15 µL. Sixteen C57BL/6J male adult mice (3.5 to 5 months old) were used, 9 in the treated group and 7 in the mock group. Seven weeks after the injury, the animals were euthanized, and the distal tibial nerve, as one of the two terminal branches of the sciatic nerve, was harvested for histological studies.

4.2. AAV2.GL injected mice

For this study, 12 C57BL/6J male mice were used, equally distributed into four experimental conditions being control, scAAV2-CMV-GFP, scAAV2.GL-CMV-GFP, and scAAV2.GL-CAG-GFP. The viral administration was via intravitreal injection with a 2×10^9 viral genomes/animal dose. After 5 weeks of administration, the animals were sacrificed, and the retinas were harvested.

5. Histological analysis

5.1. Immunofluorescence

5.1.1. Rat DRGs immunofluorescence and morphometric neurite analysis

At 9 DIV, DRGs were fixed and processed for immunofluorescence using a rabbit primary antibody anti-PGP 9.5 (1:750, Protein gene product 9.5, UCHL1, CL755GAP, Cedarlane). A secondary Alexa Fluor 595 anti-rabbit antibody (1:200, A-21207, Invitrogen, Life Technologies) was used. Slides were mounted, analyzed under a microscope (Olympus BX51), and representative images were taken. For each DRG explant, the three images with the greatest number and length of neurites were chosen for analysis. Before the image analysis, preprocessing was applied to remove the background and obtain a better neurite definition. The measurement of the neurite density and the 10 longest neurites was quantified manually with the Freehand Line tool in Fiji software, saving the respective regions of interest (ROIs). Additionally, neurite intersections, measured at 50 µm intervals from the DRG explant, were analyzed using Neurite-J (version 1.1), following the approach outlined by Torres-Espín et al. (59).

5.1.2. Whole-mount retinal immunofluorescence

To assess viral biodistribution, retinas were dissected in PBS and fixed in 10% neutral buffered formalin (NBF) for 1 h at room temperature and then overnight at 4 °C. Each retina was transferred into a 24-well plate, washed with PBST (PBS + 0.1% Triton X-100), and then permeabilized, followed by more washes. The samples were incubated overnight in wash buffer with 10% NGS at 4 °C with primary antibodies against GFAP (rat, ThermoFisher Scientific, 1:1000), β-tubulin III (rabbit, Sigma, 1:500), and NeuN (chicken, Sigma-Merck, 1:400). After three washes, Alexa Fluor 647 goat anti-rat (Invitrogen, 1:1000), Alexa Fluor 568 goat anti-rabbit (Molecular Probes, 1:1000), and Alexa Fluor 568 goat anti-chicken (ThermoFisher Scientific, 1:1000) secondary antibodies were applied overnight at 4 °C. Retinas were mounted with DAPI Fluoromount-G (ThermoFisher Scientific) after final washes. Images of the whole retina were acquired with confocal microscopy (Zeiss LSM 980). The endogenous GFP signal was quantified using Fiji software.

5.1.3. Toluidine blue staining of distal tibial nerve sections and quantification

The distal tibial nerve samples were sent to the Servei de Microscòpia i Difracció de Raigs X (SMiDRX) for inclusion in resin epoxy (EPON), semi-thin cut (1 µm), and staining with toluidine blue to stain myelin. The semi-thin sections were analyzed with a microscope (Olympus BX51) and quantified with Fiji software. The total nerve area and perimeter were manually measured in images at 40x magnification. The interior and exterior perimeter of each axon were manually delineated in 100x mosaic images, using the Freehand selection tool to calculate axonal density, axon size diameter, myelin size diameter, and g-ratio. A custom macro for Fiji was developed (Fig. 3), which automatically renames ROIs, saves their measurements (number of axons, whether it is the internal or external measurement, area, and perimeter). Additionally, this macro automatically exports a ZIP file with all the ROIs and a CSV file with all the measurements.

```
// Clear previous results and ROI Manager
run("Clear Results");
roiManager("Deselect");

// Total number of ROIs
n = roiManager("count");
if (n % 2 != 0) exit("Odd number of ROIs. They must come in interior/exterior pairs");

// Get base name of the image without extension
title = getTitle();
dotIndex = lastIndexOf(title, ".");
if (dotIndex > 0) {
    baseName = substring(title, 0, dotIndex);
} else {
    baseName = title;
}

totalAxons = n / 2;

for (i = 0; i < n; i += 2) {
    axonIndex = i / 2 + 1;

    // Rename interior ROI
    roiManager("select", i);
    roiManager("rename", "axon" + axonIndex + "_in");
    run("Measure");
    area_in = getResult("Area", nResults - 1);
    perim_in = getResult("Perimeter", nResults - 1);

    // Rename exterior ROI
    roiManager("select", i + 1);
    roiManager("rename", "axon" + axonIndex + "_out");
    run("Measure");
    area_out = getResult("Area", nResults - 1);
    perim_out = getResult("Perimeter", nResults - 1);

    // Save data into the results table
    setResult("Axon#", axonIndex - 1, axonIndex);
    setResult("Area_in", axonIndex - 1, area_in);
    setResult("Area_out", axonIndex - 1, area_out);
    setResult("Perim_in", axonIndex - 1, perim_in);
    setResult("Perim_out", axonIndex - 1, perim_out);
}
updateResults();

// Ask user to choose a folder to save the ZIP file
path = getDirectory("Choose a Directory to Save ZIP");

// Name of the ZIP file
zipName = baseName + "_rois.zip";
zipPath = path + zipName;

// Save ROIs in the chosen folder
roiManager("Deselect");
roiManager("Select All");
roiManager("Save", zipPath);

print("ROIs saved to file: " + zipPath);
```

Figure 3: Customized Fiji macro for axonal quantification in Toluidine blue-stained tibial nerve sections.

6. Gene expression analysis

6.1. RNA extraction and quantification

Each sample was homogenized with a metallic bead and QIAzol reagent (500-800 µL depending on the tissue, QIAGEN) in a TissueLyserLT (QIAGEN) for three rounds of 6 min at 50Hz. Samples were centrifuged for 10 min at 12.000g at 4 °C, and the supernatant was transferred to a clean eppendorf. After a 5-minute incubation at room temperature, chloroform (0.2 mL/mL QIAzol, Panreac AppliChem) was added, followed by a 15-minute centrifugation at 12.000g at 4 °C. The aqueous phase was recovered and precipitated with isopropanol (0.5 mL/mL QIAzol, Panreac AppliChem). The pellet was washed with 75% ethanol (1 mL/mL QIAzol, Scharlau), centrifuged, and resuspended in RNase-free water. RNA concentration was measured with the EzDrop 1000 micro-volume spectrophotometer (Blue-Ray Biotech), and then stored at -80 °C.

6.2. DNase protocol and cDNA synthesis

To remove the genomic DNA from RNA samples for qPCR, the RNase-free DNase I kit was used (ThermoFisher), per the manufacturer's instructions. For the complementary DNA (cDNA) synthesis, the iScript™ cDNA Synthesis Kit (Bio-Rad) was used following the manufacturer's instructions to obtain

either 1000 ng in a final volume of 20 µL or 500 ng in 24 µL, depending on the tissues. The cDNA was stored at -20 °C.

6.3. Quantitative polymerase chain reaction (qPCR) and data analysis

Quantitative PCR (qPCR) analyses were run in 384-well plates, with each plate containing samples from the same experiment and tissue. Two multiplex mixes with TaqMan technology, the first for *RER1* and *sKL*, and the second for *RPLP0* and *mKL*, were prepared. The samples were loaded in triplicate for the first mix and in duplicate for the second mix. For each reaction, 8 µL of multiplex master mix (5 µL of SensiFAST™ Probe No-ROX Kit (Ref. BIO-86005, Ecogen), primers, and probes at their corresponding concentration), and 2 µL of cDNA were used. A no-template control (NTC) for each mix was also added. Plates were sealed and centrifuged (900 rpm for 1.5 min) before starting the program, consisting of 15 min at 50 °C, 1 min at 95 °C, then 39 cycles of 10 s at 95 °C and 1 min at 60 °C in CFX384 Touch Real-Time PCR System (Biorad).

PCR primer efficiencies were calculated beforehand based on serial dilutions of cDNA. Efficiencies were: *RPLP0* = 1.95, *RER1* = 1.83, *mKL* = 2.02, and *sKL* = 1.97. *RPLP0* and *RER1* genes were used as reference genes. The Pfaffl method (60) was used for qPCR data analysis.

Table 3: Primer sequences for RT-qPCR

qPCR primers	Forward (5' – 3')	Probe	Reverse (3' – 5')
RPLP0 (ribosomal protein lateral stalk subunit P0)	ATGGGTACAAGCGCG TCCTG	HEX – TGTGGAGACTGAGTACACCTTCCCA - BHQ-1	AGCCGCAAATGCAGA TGGATC
RER1 (retention in endoplasmic reticulum sorting receptor 1)	TACATTGTGACCTACG CCTTG	HEX - TGATGGAAGACTCAGATGACGGCCC - BHQ-1	CGAAATTCCTCATTCT GTTTGGTT
mKL (membrane Klotho)	TACGGAGACCTCCCGA TGTA	Cy5 – ATGGAATCGATGATGACCCCCACGC - BHQ-2	CGCAAAGTAGCCACA AAGGT
sKL (soluble Klotho)	CAATGGCTTTCCTCCTT TACC	6FAM - AGGGACATTTCCCTGTGACTTTGCTTGG - BHQ-1	GAGGCCGACACTGGG TTTTG

7. Statistical analysis

The analyses of the in vivo experiments were all carried out blinded to treatment received, to avoid bias. GraphPad Prism version 9.3.1 (GraphPad Software) was used for statistical analysis. Data are displayed as mean ± SEM (standard error of the mean), and the statistical significance was considered at values of $p \leq 0.05$.

The Shapiro-Wilk test was used for checking normal distribution, and the F-test for homogeneity of variances. Under normality and homoscedasticity assumptions, to compare two experimental groups, a two-tailed unpaired Student's t-test was performed. Comparisons between more than two groups and one factor were performed with the one-way analysis of variance (ANOVA), followed by Holm-Šídák multiple comparisons post-hoc test. Two-way ANOVA was performed for comparisons between more than two groups with two factors and post-hoc Holm-Šídák test. Outliers in the qPCR experiments were considered as values ±1.5 SD from the mean of the logarithmic values after applying the Pfaffl equation.

RESULTS

1. Klotho is downregulated after sciatic nerve resection

Klotho levels are known to decrease during aging and neurodegenerative diseases (34,35). To evaluate whether PNI alters endogenous Klotho levels, we analyzed its expression in hindlimb muscles and spinal cord tissues from mice subjected to sciatic nerve resection or sham surgery. Animals were euthanized, and tissues were harvested 7 or 28 dpi (Fig. 4A).

The sciatic nerve anatomically branches into the tibial nerve and the common peroneal nerve (61). While the tibial nerve is responsible for innervating the gastrocnemius (GM) and Soleus (Sol), the common peroneal nerve innervates the Tibialis Anterior (TA) and Extensor Digitorum Longus (EDL), among others. In addition, the sciatic nerve provides sensory innervation to most of the posterior lower limb and contributes with its branches, such as the medial and lateral sural nerves, which originate from the tibial and common peroneal nerve, respectively (61). To assess how the lack of innervation affects tissues that depend on sciatic nerve innervation, representative hindlimb muscles (TA, GM, Sol, and EDL) and the lumbar spinal cord were dissected, and quantitative PCR (qPCR) was performed to analyze gene expression of both mKL and sKL. To ensure the reliability of qPCR assays, qPCR conditions were optimized, and primer efficiency values were calculated (ranging between 83-102 %).

Since no differences were detected between sexes, values from males and females were analyzed collectively. In the hindlimb muscles, a marked reduction in mKL levels was observed in GM (-0.49-fold at 7 dpi) and in EDL (-0.36-fold at 7 dpi; -0.88-fold at 28 dpi), compared with sham animals of the same age (Fig. 5A). Interestingly, in the TA, mKL expression tended to increase at 7 dpi, although this was followed by a reduction at 28 dpi, which did not reach statistical significance. In Sol, mKL expression remained unchanged. For sKL levels in hindlimb muscles, a significant decrease was detected in GM (-0.40-fold at 7 dpi; -0.53-fold at 28 dpi), Sol (-0.45-fold at 28 dpi), and EDL (-0.71-fold at 28 dpi) (Fig. 5B). There was a tendency toward a reduction in sKL expression in TA, but not statistically significant. In the spinal cord, mKL was statistically significantly downregulated at 7 dpi (-0.27-fold) (Fig. 5C), while sKL expression followed a trend towards downregulation (Fig. 5D).

After sciatic nerve resection, we observed a marked reduction in mKL and sKL in hindlimb muscles, whereas in the spinal cord, only mKL showed a statistically significant reduction. These results indicate the differential regulation and potential roles of each Klotho isoform after PNI.

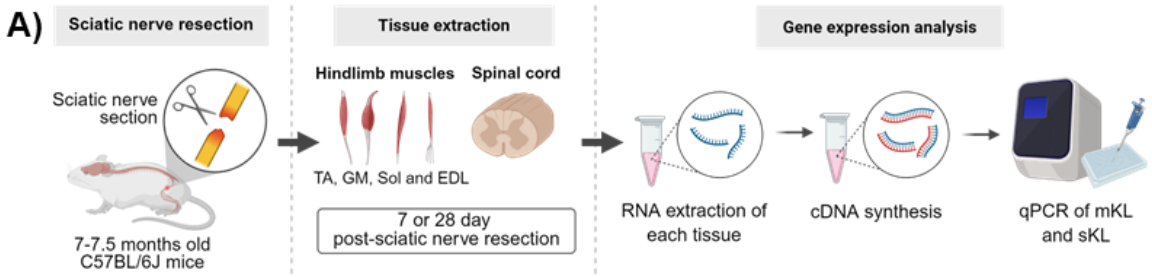

Figure 4: Experimental design for the sciatic nerve resection model and the gene expression analysis *(Designed with Biorender).*

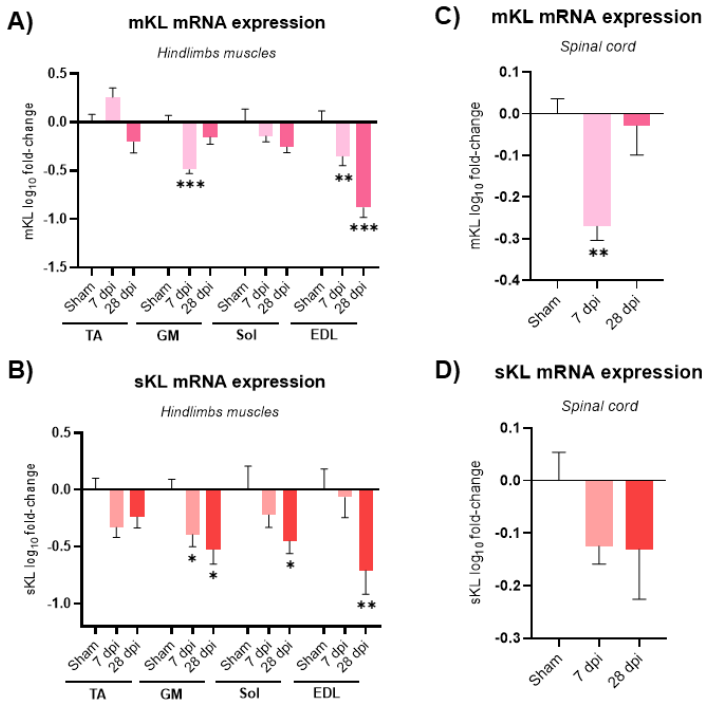

Figure 5: mRNA expression of Klotho isoforms is reduced after sciatic nerve resection in 7-month-old mice. Bar plots showing the log_{10} fold-change in mRNA expression of mKL (A) and sKL (B) in hindlimb muscles, compared to Sham mice on the respective day post-surgery. mKL (C) and sKL (D) mRNA expression in the spinal cord. Results are expressed as mean ± SEM (n= 7-8 Sham, n= 5-7 resection). Two-way ANOVA for muscles, One-way ANOVA for spinal cord, with the post-hoc Holm-Šídák tests, *p≤ 0.05, **p<0.01.

2. Klotho isoforms show differential regulation after sciatic nerve crush

To evaluate endogenous Klotho levels in a more clinically frequent PNI, we used a sciatic nerve crush model, which is less severe, preserves nerve continuity, and allows spontaneous regeneration. At 1, 3, 7, 14, and 28 dpi, animals were euthanized and both contralateral and ipsilateral tissues were harvested, including the lumbar spinal cord, DRGs, sciatic nerve, and hindlimb muscles (Sol and GM) (Fig. 6A). The gene expression of mKL and sKL was analyzed with qPCR.

As no sex differences were observed, data were combined. In the lumbar spinal cord, mKL mRNA expression was notably reduced on the contralateral side (-0.38-fold at 7 dpi; -0.25-fold at 14 dpi), while the ipsilateral side remained unchanged compared to sham animals (Fig. 6B). At 28 dpi, mKL levels tended to increase. In contrast, sKL expression appeared to increase at 1 and 3 dpi, and then tended to decline from 7 dpi onward, with no differences between the contra- and ipsilateral sides (Fig. 6C). In the DRG, mKL expression significantly decreased at 1 dpi on the ipsilateral side and approached physiological levels onwards (Fig. 6D). sKL levels tended to increase at 3 dpi, followed by a progressive reduction to sham levels (Fig. 6E). In the sciatic nerve, mKL was downregulated on the proximal and distal ipsilateral segments, achieving statistical significance at 1, 3, 7, and 14 dpi (Fig. 6F). At 28 dpi, when no proximal and distal stumps are distinguishable, mKL levels tended to surpass physiological levels. On the contrary, sKL expression levels slightly and non-significantly increased on the proximal stump, whereas the ipsilateral distal region showed the strongest increases, statistically significant at 1-, 3-, 7-, 14-, and 28 dpi (Fig. 6G). In the hindlimb muscles, mKL expression in the Sol muscles did not show a clear pattern; only a trend for an increase was observed in the ipsilateral muscles 1-dpi and for the contralateral muscle at 14- and 28-dpi (Fig. 6H). sKL expression was strongly increased at 1 dpi; however, it rapidly returned to sham levels (Fig. 6I). In contrast, in the GM, mKL expression was consistently reduced across all time points following crush injury (Fig. X6J). On the

other hand, sKL expression in the GM showed a transient increase at 1 dpi, followed by a slight decline compared with sham animals, although these changes did not reach statistical significance (Fig. 6K).

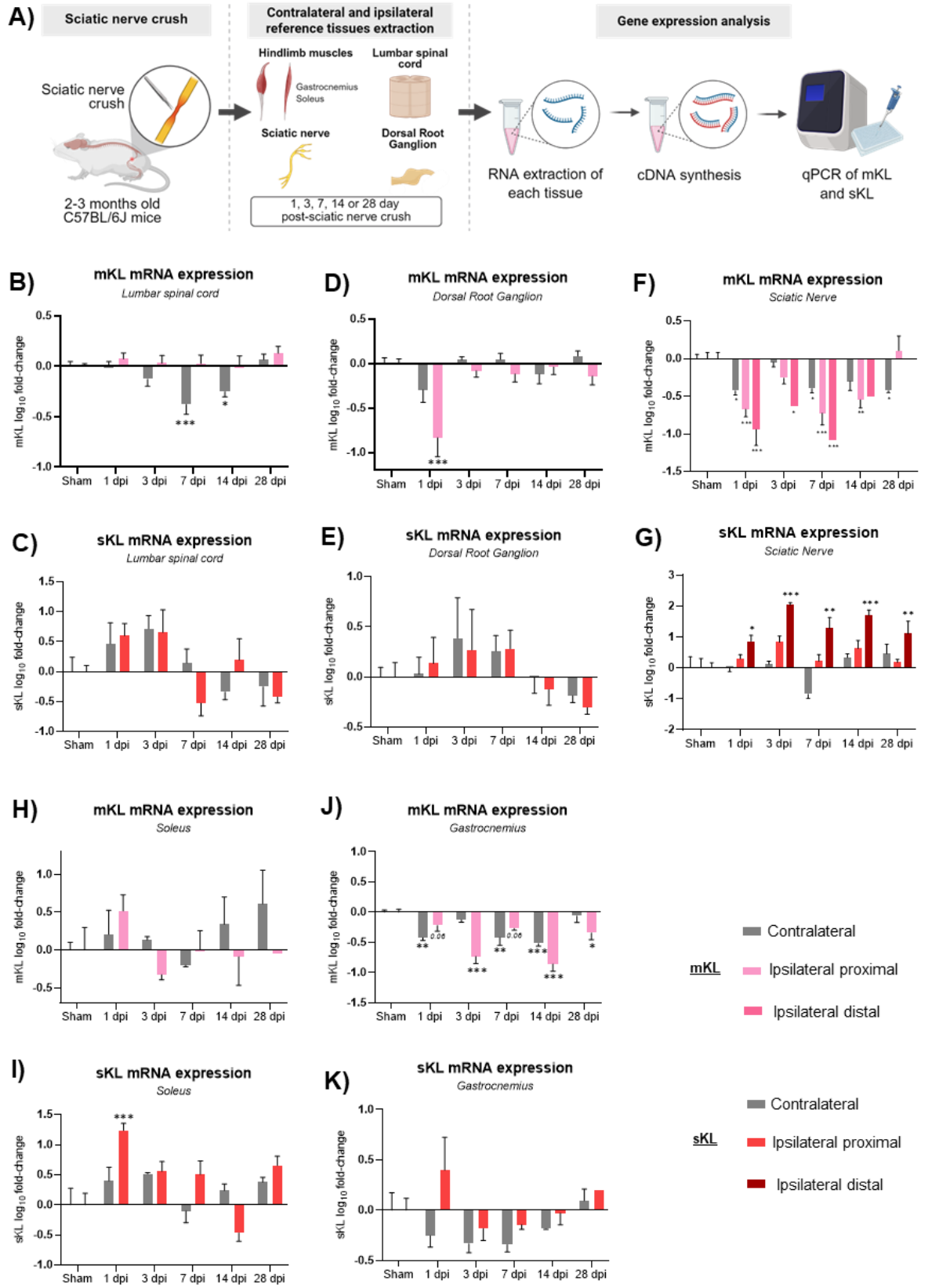

Figure 6: mRNA expression of Klotho isoforms shows differential regulation after sciatic nerve crush in 2-3-month-old mice. (A) Experimental design of sciatic nerve crush model and gene expression analysis *(Designed with Biorender).* $\log_{10}$ fold-change expression of mKL and sKL in the lumbar spinal cord (B, C); lumbar DRGs (D, E); sciatic nerve (F, G); Soleus (H, I); and Gastrocnemius (J, K). Comparison to Sham mice on the respective day post-surgery. Results are expressed as mean ± SEM (n= 7-8 Sham, n= 5-7 mice crush). Two-way ANOVA, with the post-hoc Holm-Šídák tests, *p≤ 0.05, **p<0.01, ***p≤ 0.001.

3. AAV-mediated sKL overexpression promotes neurite outgrowth in rat DRG organotypic culture

To evaluate the potential of Klotho in promoting neurite growth, we used an *in vitro* organotypic culture model of rat DRGs from newborn pups. To this end, Klotho was overexpressed either by viral vectors (AAV9-CMV-mKL and AAV9-CMV-sKL) or recombinant sKL protein in the media. After extraction, DRGs were cultured on a three-dimensional collagen matrix and treated accordingly (Fig. 7A). At 9 DIV, explants were fixed and processed for immunofluorescence labelling the neurofilament marker PGP 9.5, allowing visualization of growing neurites.

We manually measured neurite density relative to the perimeter of each DRG explant, as no significant differences in explant perimeter were detected among groups (data not shown). The recombinant sKL-treated groups showed a similar number of neurites to the PBS-treated control group (17.21 ± 8.49 neurites/µm); on the contrary, AAV-mKL-treated explants exhibited a trend for more neurites (25.43 ± 8.26 neurites/µm), and AAV-sKL-infected DRGs had a statistically significantly higher density of neurites compared to the control group (Fig. 8A and 8B). Neurite density approximately doubled in AAV-sKL explants compared to the untreated control (29.49 neurites/µm ± 9.19 in AAV-sKL vs. 15.53 ± 10.42 neurites/µm in control). From each DRG, we also manually measured the longitude of the 10 longest neurites. Across the different treatments, no significant differences were found regarding the neurite length, with average values ranging from 690 to 870 µm (Fig. 8C).

Since the most prominent differences were found in the AAV-sKL group, manual analyses were complemented with Neurite-J analysis, a Fiji plugin that allows for quantification of the number of intersections at regular intervals from the DRG explant. Consistent with the manual measurements, this analysis demonstrated a statistically significant increase in the number of intersections in the AAV-sKL-treated group within the 50–300 µm length range (Fig. 8D). Higher number of intersections were detected in the AAV-sKL group compared to controls for most of the distances studied, which was also reflected as a statistically significant larger area under the curve (Fig. 8E). The maximum outgrowth distance of the longest neurites was comparable across conditions, reaching 850 µm in the control group and 950 µm in the AAV-sKL group. This further indicates that the observed effect of Klotho in rat DRG organotypic cultures did not significantly affect neurite length but rather promoted the growth of more neurites.

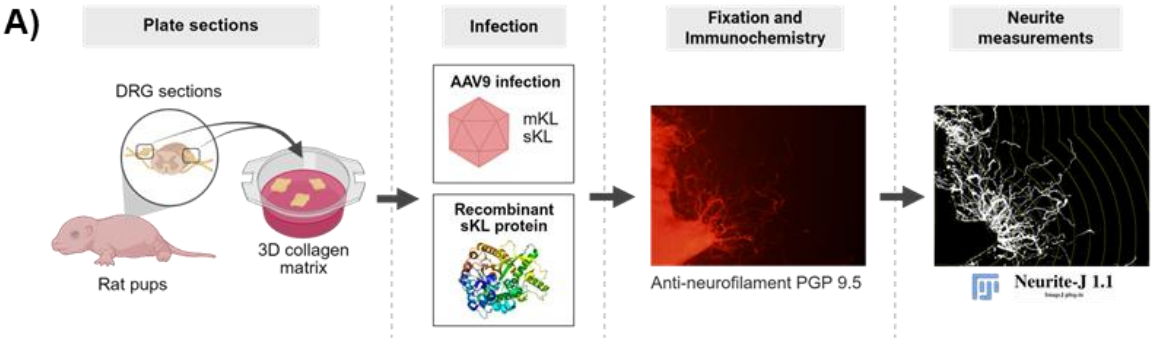

Figure 7: Graphical experimental design of rat DRG organotypic cultures *(Designed with Biorender).*

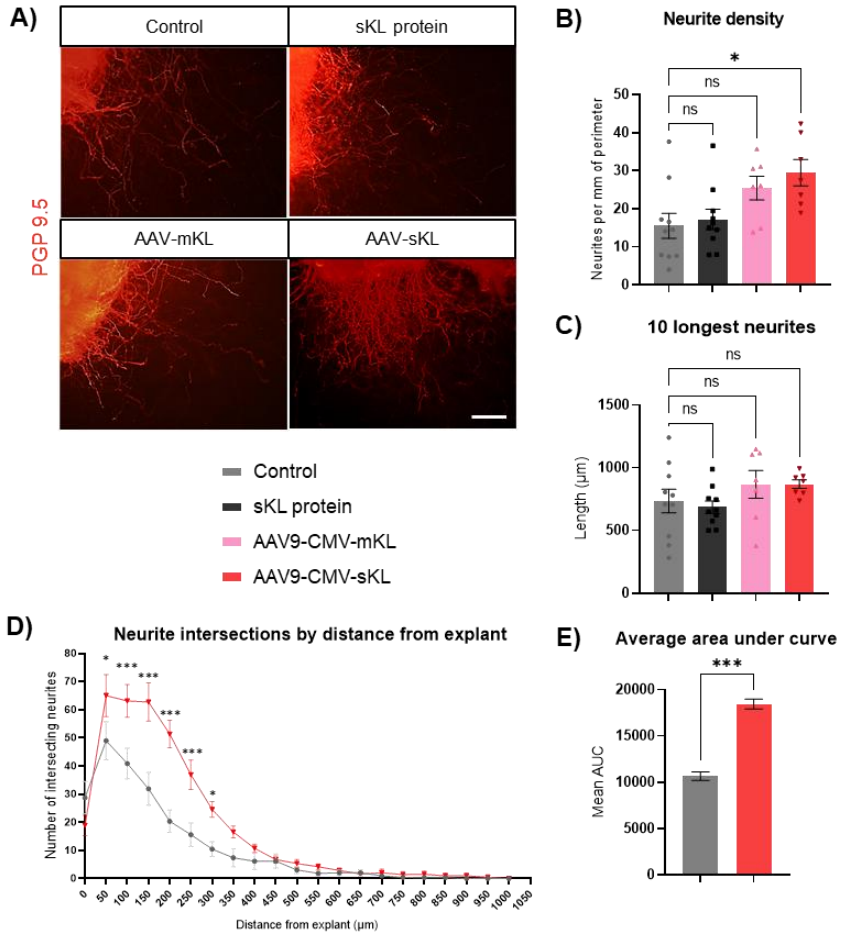

Figure 8: AAV-mediated sKL overexpression doubles neurite density in rat DRG organotypic cultures. (A) Klotho concentration was increased using recombinant sKL protein or overexpression with AAV9 vectors (AAV9-CMV-mKL and AAV9-CMV-sKL) in DRG cultures. Neurites were labeled with the PGP 9.5 antibody. Scale bar**:** 100 µm. Histograms show, for each DRG, the neurite density normalized by perimeter (B) and the length of the 10 longest neurites (C). The number of intersections at 50 µm intervals from the DRG explant was analyzed using Neurite-J (D) with the corresponding area under the curve (E). Results are expressed as mean ± SEM (n=10 DRGs for control and sKL protein, n=7 DRGs for AAV9-CMV-mKL and AAV9-CMV-sKL). One-way ANOVA, with post-hoc Holm-Šídák tests, *p≤ 0.05, ***p≤ 0.001.

4. Klotho enhances axonal regeneration and remyelination after sciatic nerve section

To evaluate the regenerative and remyelination capacity of Klotho in PNI, we used a “cut-and-paste” sciatic nerve injury model in mice. This injury is characterized by a complete sciatic nerve section reglued using fibrin glue, composed of fibronectin, fibrin, and thrombin (Fig. 9A). Immediately after the injury, intrathecal injections (L3 or L4 segments) of scAAV9 were administered by certified personnel with the secreted form of Klotho (sKL) or a stuffer sequence as control (Null) under the CMV promoter.

This therapeutic assay involved adult male C57BL/6J mice between 3.5 and 5 months of age, which received a dose of 1.5×10^{11} vg of scAAV9-CMV-sKL or scAAV9-CMV-Null vectors. The intrathecal administration of AAV9 vectors efficiently transduces the spinal cord and the brain, as well as distributes into PNS regions, targeting neurons and glia (62,63). Seven weeks after viral administration, animals were euthanized, and the distal tibial nerves extracted. EPON-embedded nerves were sectioned and stained with Toluidine Blue for morphometric analysis. Analyses were performed in Fiji software, using a custom macro developed to facilitate large-scale data processing (see Methods).

The surface and total perimeter of the tibial nerve were not statistically different between sKL-treated (32,944.38 µm² and 783.83 µm, respectively) and mock-treated animals (29,886.22 µm² and 663.82 µm, respectively) (Fig. 9B, 9C, and 9D). However, sKL-treated animals showed a tendency toward increased nerve area and perimeter.

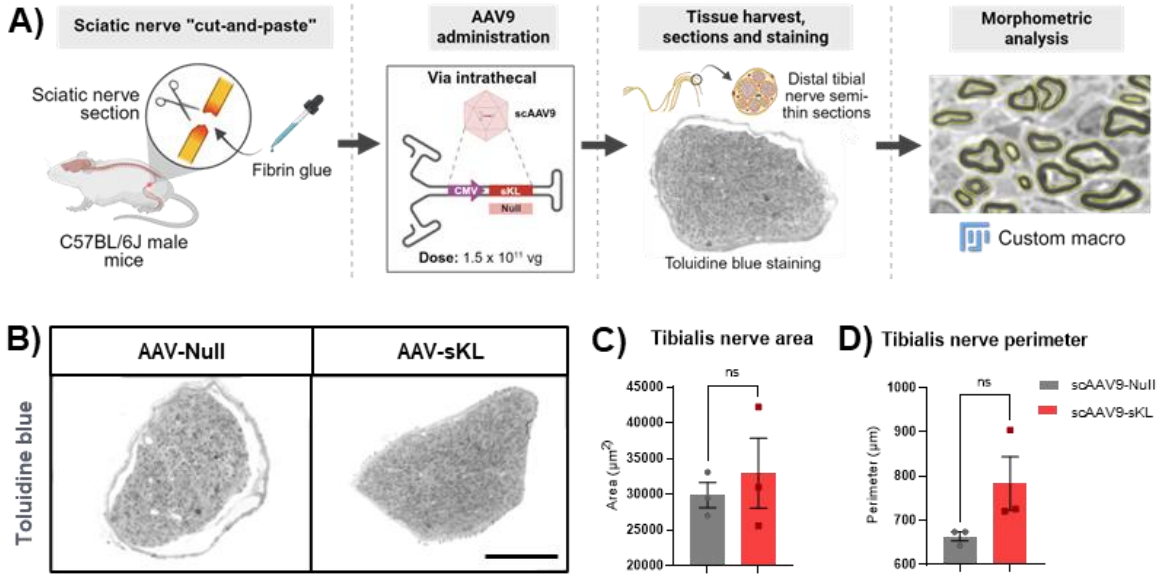

Figure 9: Sciatic "cut-and-paste" model and morphometric assessment of tibial nerve after scAAV9-mediated sKL overexpression. A) Graphical experimental design of sciatic nerve "cut-and-paste" model *(Designed with Biorender).* Klotho was overexpressed with intrathecal administrations of scAAV9-CMV-sKL and compared to the mock group administered with scAAV9-CMV-Null, a stuffer sequence as a control. The most distal region of the tibial nerve was harvested, sectioned, and stained with Toluidine Blue for morphometric analysis. Representative images of the distal tibial nerve for each condition. Scale bar**:** 100 µm (B). Histograms show the quantification of the total tibial nerve area (C) and perimeter (D). Results are expressed as mean ± SEM (n=3 nerves per treatment). Two-tailed unpaired Student's T-Test.

To analyze axonal density, size, and myelination, images at higher magnification (100×) were used (Fig. 10A). Thus, the number of axons revealed a statistically significant increase in sKL-treated mice (372.5 ± 9.15 axons/10,000 µm²) compared to untreated animals (198.09 ± 5.95 axons/10,000 µm², Fig. 10B). Notably, axons were larger in the sKL-treated group (Fig. 10C), as axonal diameter was statistically significantly increased among the 2,621 axons counted in the sKL group, compared to the 1,757 axons from the control group. The most common axonal diameter range was 2–6 µm in sKL-treated mice, whereas in untreated animals it was 1.5–5 µm, demonstrating a clear shift in axon diameter distribution to larger calibers (Fig. 10D). In addition, the myelin sheath was statistically significantly thicker in the sKL-treated group (Fig. 10E). In sKL-treated mice, the myelin sheath had a mean thickness of 0.65 ± 0.21 µm compared to that of the control, with 0.57 ± 0.17 µm. The most prevalent myelin thickness was 0.6-0.7 µm (18.43%) in sKL-treated mice, and in control mice, it was 0.4-0.5 µm (25.2%) (Fig. 10F).

Moreover, as a parameter to evaluate axonal myelination, the g-ratio index is used to normalize myelin thickness by axonal caliber. It is calculated by dividing the axon diameter by the entire fiber diameter. For efficient nerve conduction velocity in mice, a g-ratio of 0.6 is considered optimal (64). There is a negative correlation between myelin thickness and the g-ratio. Consistent with the results obtained with axonal diameter and myelin thickness, g-ratio analysis further supported that AAV-mediated sKL overexpression improves tibial nerve axonal regeneration in sciatic nerve cut-and-paste. sKL-treated mice presented a statistically lower g-ratio (0.62), which is close to the optimal value in mice, whereas untreated animals had a higher g-ratio (0.78), suggesting hypomyelination (Fig. 10G).

Indeed, although the surface and total perimeter of the tibial nerve were not significantly different between sKL-treated and untreated mice, axon density was higher and axons were larger and more myelinated in the sKL-treated group, which resulted in a lower g-ratio.

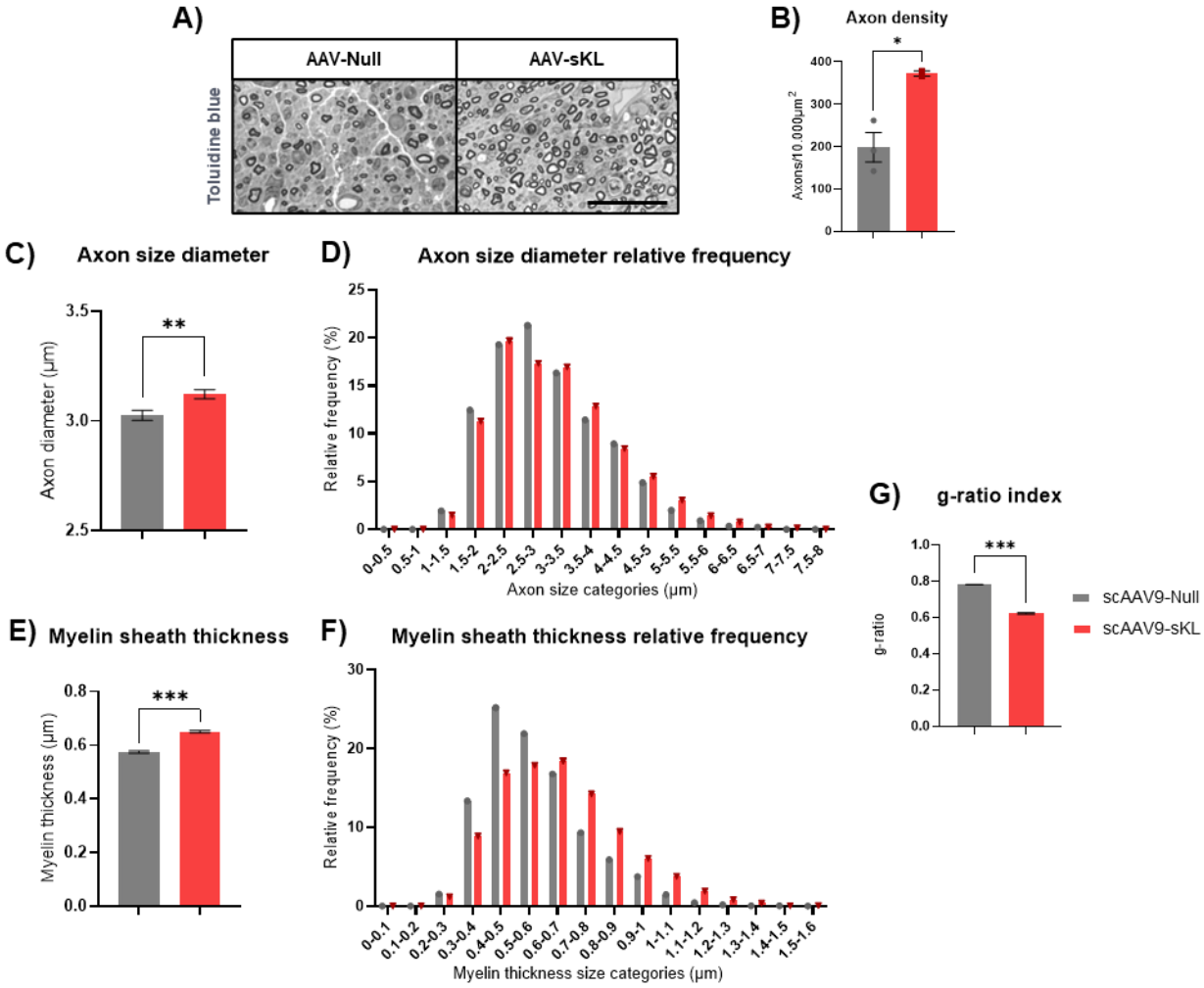

Figure 10: scAAV9-CMV-sKL intrathecal administration enhances axonal regeneration and remyelination in the tibial nerve after sciatic nerve cut-and-paste injury. (A) Representative sections from the tibial nerves from mice treated with scAAV9-CMV-sKL or scAAV9-CMV-Null. Scale bar: 30 µm. The number of axons normalized by nerve perimeter (B), the axon size diameter (C) with its relative frequency (D), and myelin sheath thickness (E) with its relative frequency (F) were quantified using the custom macro for Fiji. The g-ratio was calculated for both conditions (G). Results are expressed as mean ± SEM (n= 2,621 axons in scAAV9-CMV-sKL and n= 1,757 axons in scAAV9-CMV-Null). Two-tailed unpaired Student's T-Test, *p≤ 0.05, **p<0.01, ***p≤ 0.001.

5. Novel AAV2.GL capsid efficiently transduces retinal neurons

This study represents a first step to evaluate viral tropism in the mouse retina using modified AAV2 capsids. The objective of this study was to select the capsid with greater tropism toward retinal neurons to deliver sKL as a therapeutic transgene in future studies to the *Wfs*-deficient rat model with optic nerve atrophy (31).

The natural serotype AAV2 has tropism for the retina, however, transduction of RGCs might be more challenging, which is why novel capsids have been engineered to increase vector transduction efficiency in neurons and photoreceptors. Through a site-directed strategy, we inserted the GLSPPTR 7-mer, a specific sequence described by Pavlou et al. (56), between residues N587 and R588 of the VP3 sequence in the AAV2 capsid (Fig. 11A). The PCR product was digested with DpnI, transformed into competent cells, and confirmed colonies were sequenced and used to amplify the plasmid DNA. We produced the viral vectors scAAV2-CMV-GFP, scAAV2.GL-CMV-GFP and scAAV2.GL-CAG-GFP, using

GFP as a reporter to assess retinal transduction and compare transduction efficiency between capsids, and also the effect of the CAG promoter. These vectors were administered intravitreally at the same dose (2×10^9 vg/animal) in mice, and their retinas were harvested after five weeks of administration.

First, we assessed transduction efficiency between capsids in the retina, comparing AAV2 and AAV2.GL capsids with the control of the CMV promoter. A tendency towards more specific neuronal transduction with the AAV2.GL capsid was observed (Fig. 11B, 11C). This suggests that, with the same promoter, AAV2.GL capsid can enhance neuronal transduction. Secondly, the effect of the CAG promoter was evaluated. We observed higher transduction with the scAAV2.GL vector under the ubiquitous CAG promoter compared with AAV2.GL under the control of the CMV promoter at the examined time point (Fig. 11B). Moreover, scAAV2.GL-CAG-GFP showed a significant increase in colocalization (32.75%) of GFP with the neuronal marker Tuj1 (anti-βIII-tubulin antibody) (Fig. 11C). Although the difference was not statistically significant, scAAV2.GL-CMV-GFP showed greater colocalization (19.87%) than scAAV2-CMV-GFP, which transduced less efficiently (11.35%).

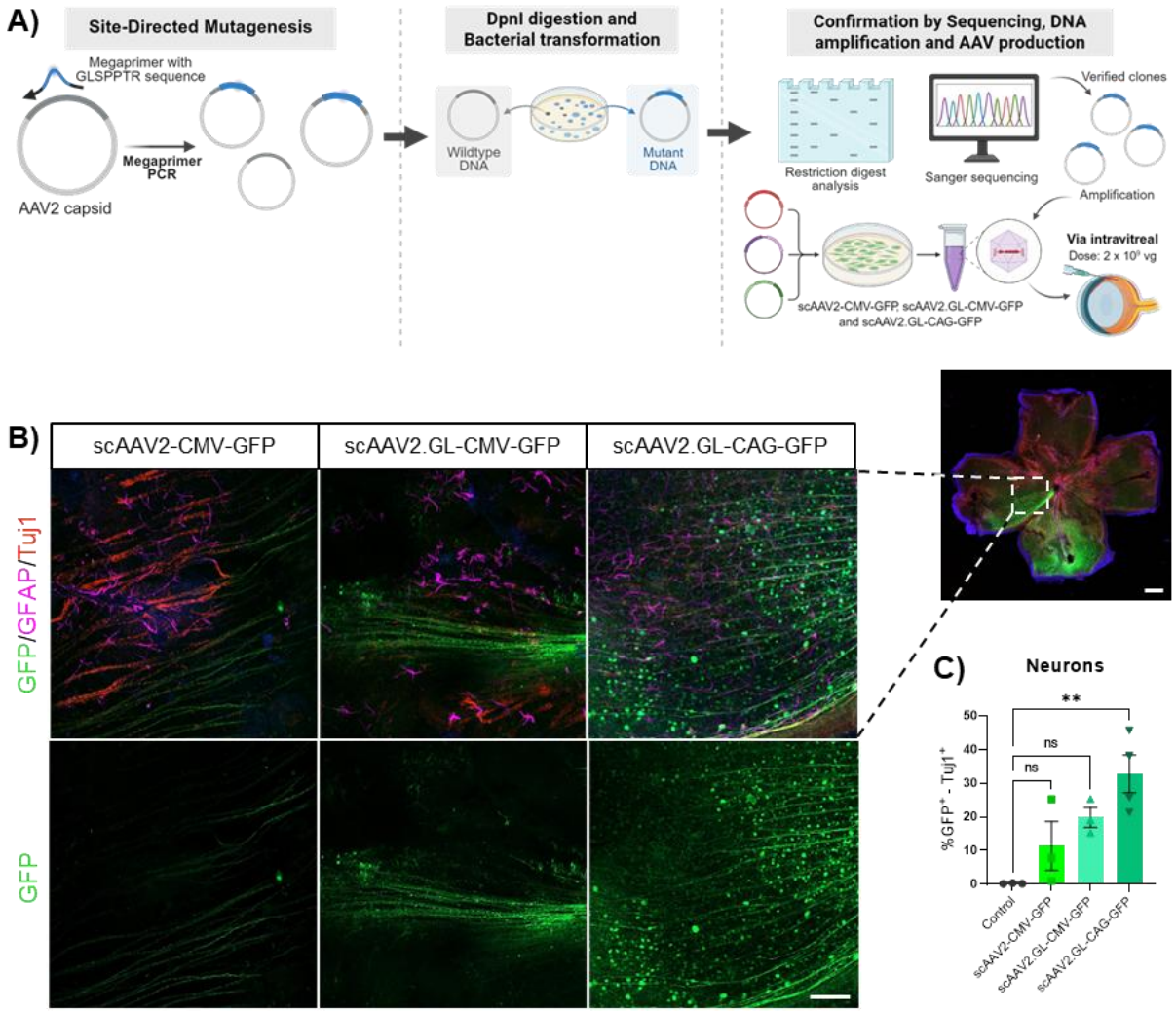

Figure 11: AAV2.GL-CAG-GFP efficiently transduces retina and preferentially co-localizes with retinal neurons. (A) Graphical experimental design for the generation of pscAAV2.GL-CAG-GFP and pscAAV2.GL-CMV-GFP *(Designed with Biorender)*. An overlapping PCR strategy introduces the GLSPPTR sequence into the AAV2 capsid with a megaprimer-directed mutagenesis. After DpnI digestion to remove the methylated parental AAV2 capsid plasmid and bacterial transformation, the plasmid DNA was screened and amplified. Confocal slides of the whole-mount retinal immunofluorescence from mice injected with AAV showing GFP expression in green (B). Scale bar: 100 µm (left), 500 µm (right). Quantification of GFP-positive neurons (C), showing a statistically significant ~32% colocalization in scAAV2.GL-CAG-GFP. Results are expressed as mean ± SEM (n=3 animals per treatment). One-way ANOVA, **p<0.01.

DISCUSSION

Currently, after severe injuries in the PNS or CNS, full motor and sensory recovery is rarely achieved. Existing therapeutic strategies include non-surgical approaches, surgical interventions, pharmacological approaches, and the administration of growth factors. However, these strategies still fail to address the complex regeneration environment in the PNS and the CNS, and no effective approach is available for nervous injuries affecting both systems. In this context, gene therapy using AAV viral vectors is a promising approach due to its cell-type specificity, ability to provide long-term effects without constant readministration, and less invasive surgeries, among other advantages. For these reasons, we proposed to explore the potential of AAV-mediated α-Klotho overexpression given its multifaceted effects on neuroinflammation, oxidative stress, excitotoxicity, apoptosis, and myelination, processes central to nerve regeneration.

Klotho endogenous expression in the sciatic nerve resection model

The two isoforms of the α-Klotho protein (mKL and sKL) are expressed at different levels and show distinct expression patterns depending on the tissue (35,42). Previous studies have shown a decrease in Klotho expression during aging and neurodegenerative diseases such as Alzheimer's (34). Moreover, this reduction in Klotho levels has been observed in muscle degeneration and atrophy (49,65).

We measured endogenous mRNA expression of Klotho isoforms in hindlimb muscles and spinal cord from a sciatic nerve resection model in adult C57BL/6J mice, aiming to analyze how denervation affects KL expression in these tissues. In general terms, in the examined hindlimb muscles, mKL mRNA expression was significantly reduced in the GM and the EDL, while remaining unchanged in the Sol (Fig. 5A). Interestingly, in the TA, mKL levels tended to increase at 7 dpi, followed by a reduction at 28 dpi. For sKL levels, a marked decline was detected in the GM, Sol, and EDL; whereas a tendency toward a reduction was observed in the TA (Fig. 5B). Muscles innervated by the sciatic nerve, after sciatic nerve resection, experience metabolic changes leading to a pro-inflammatory environment and muscle atrophy. The muscles in which Klotho expression was most downregulated were GM and EDL, consistent with their predominantly glycolytic fiber types, which make them more susceptible to atrophy after denervation. The TA is noteworthy, as despite being glycolytic, it exhibited a transient upregulation of mKL expression before declining, a mechanism that remains unclear. In contrast, unchanged mKL levels were detected in the Sol, which could be explained as it is an oxidative muscle with fatigue-resistant fibers (66,67). Additional factors, such as the innervation pattern or metabolism of each muscle, must be considered in the development of muscle atrophy.

In the spinal cord, mKL was significantly downregulated at 7 dpi, while sKL expression tended to decrease without reaching statistical significance (Fig. 5C, 5D). The spinal cord is not directly injured after sciatic resection; however, retrograde signals from damaged neurons result in the infiltration of immune cells and the release of pro-inflammatory cytokines and chemokines (68,69). Overall, mKL mRNA is more markedly reduced than sKL in both hindlimb muscle tissues and spinal cord after sciatic nerve resection.

Together, these results suggest that the endogenous regulation of Klotho after sciatic nerve resection depends on the cell type, tissue, age, and isoform examined, highlighting the differential regulation of Klotho following peripheral injuries. Nonetheless, to confirm these gene expression analyses, additional studies in this sciatic nerve resection model should assess mKL and sKL protein expression, as mRNA expression does not always correlate with functional protein abundance. Finally, a ddPCR (digital PCR) protocol could be considered for future assays. Based on the qPCR experience, even after checking efficiency and Cq values in different plates with control samples, variability remained higher than desired due to the low expression levels of these genes (sKL: Cq~30; mKL: Cq~27).

Klotho endogenous expression in the sciatic nerve crush model

As compression injuries are more common in clinical settings, we used the sciatic nerve crush model in adult mice (2-3 months) to evaluate endogenous Klotho levels. This type of compression injury, which rarely causes neuronal death, damages axonal and myelin structures while sparing the connective tissue and is therefore considered milder than complete resection.

After injury, in the lumbar spinal cord, mKL expression was reduced on the contralateral side at 7 and 14 dpi, with the ipsilateral side unchanged compared to sham animals (Fig. 6B). There was a trend towards an increase in mKL expression at 28 dpi. In contrast, sKL expression tended to increase at 1 and 3 dpi and then decline from 7 dpi onward, indicating opposite regulation of the two isoforms (Fig. 6C). Although the spinal cord is not directly injured in PNI, it receives retrograde signals from damaged motor neurons, leading to astrocyte and microglial activation, increased release of pro-inflammatory cytokines and chemokines (68,69). Low mKL levels are consistent with this early pro-inflammatory stage in the spinal cord, while the trend to increase at 28 dpi could be related to a resolution of inflammation. The initial increase in sKL could be related to an acute damage response.

In DRG, mKL expression was significantly reduced at 1 dpi on the ipsilateral side, returning close to physiological levels afterwards (Fig. 6D). sKL levels tended to increase until 7 dpi, followed by a progressive reduction to sham levels (Fig. 6E). Sensory neurons in DRG respond to injury with immune cell infiltration, stress response, and sometimes neuronal death (70,71). In a similar fashion to the spinal cord, the decrease in mKL levels aligns with pro-inflammatory signaling in DRG sensory neurons, whereas the initial trend toward increased sKL expression could be a short protective response.

In the sciatic nerve, mKL was significantly downregulated in ipsilateral proximal and distal segments from 1 to 14 dpi (Fig. 6F). Contrarily, sKL expression tended to slightly increase in the ipsilateral proximal region, whereas the ipsilateral distal region showed the strongest increases (Fig. 6G). The sciatic nerve is the site of injury in this model, and at 24-48h post-injury, Wallerian degeneration occurs distal to the injury site. This degeneration involves the disruption of both axonal and myelin structures (14). The reduction in mKL levels, both in the distal and proximal segments, can be related to axonal degeneration and an associated pro-inflammatory environment. The increase in sKL in the distal segment could be related to a compensatory response, either due to the severity of degeneration in this region or increased expression by infiltrating macrophages.

In the hindlimb muscles, specifically in the Sol, mKL expression was highly variable (Fig. 6H), while sKL expression increased significantly in the ipsilateral side at 1 dpi and rapidly returned to sham levels (Fig. 6I). In contrast, in GM, mKL levels decreased markedly on both the ipsilateral and contralateral

sides across all time points following crush injury (Fig. 6J). On the other hand, sKL levels initially appeared to increase at 1 dpi, followed by recovery to normal levels (Fig. 6K). After sciatic nerve injury, muscles undergo denervation, which leads to metabolic changes and an inflammatory environment that results in muscle atrophy due to a lack of connectivity with the distal nerve stump. These observed differences in the muscles after denervation could partially be explained by muscle fiber type. The soleus is a muscle with predominantly oxidative fibers, suggesting its response will be more adaptive, whereas the GM has more glycolytic fibers that are more vulnerable to atrophy (66,67).

In general, there are differences between these results and those observed in the sciatic nerve resection model and in adult crush. On the one hand, this could be due to the magnitude of the injury, which is greater with complete nerve resection compared to crush. Sciatic nerve resection is associated with greater neuronal loss (72), and thus, Klotho expression could be more affected since neurons represent a source of its expression. On the other hand, the age of the mice at the time of injury could also be a factor to consider, since sciatic compression in neonates is more severe than performing the same injury in adults. It has been shown that there is greater death of sensory and motor neurons during early postnatal periods, such as P3 and P5, whereas in adults, the injury barely changes the number of neurons compared to control animals (73). Previous findings from our research using a sciatic nerve crush model in neonatal mice (unpublished data), which show higher neuron death upon injury, showed mKL downregulation in hindlimb muscles while sKL remained practically unchanged. In contrast, in the spinal cord, sKL was reduced, and mKL expression did not show significant changes, both at 14 dpi. Therefore, crush injury in adults may allow for a partial compensatory response in Klotho expression, which is not feasible after complete resection. Conversely, in neonates, even a crush injury results in a stronger reduction due to their higher vulnerability and neuronal death.

Finally, on the more technical side of qPCR, it is important to highlight the difficulty of measuring the expression of Klotho isoforms at the endogenous level outside the kidney and the brain, where it is predominantly expressed. As future perspectives, Klotho expression at the protein level after sciatic nerve crush needs to be addressed, with ELISA, immunohistochemistry, or Western Blot, methods that may present technical difficulties, to complement these mRNA analyses.

sKL overexpression promotes neuritogenesis in rat DRG organotypic culture

Several experimental models are available to study sensory neuron regeneration. Rat DRG organotypic cultures enable the modeling of the structural organization of the tissue from which it is extracted and reproduce cellular interactions (28). In addition, axonal growth is enhanced in the culture with collagen as an extracellular matrix organic hydrogel (74). Another advantage of this model is the three-dimensional approach, which is difficult to obtain with conventional *in vitro* cultures. Remarkably, for this rat DRG organotypic culture, neurotrophic factors are not necessarily required. Since our objective is to study how Klotho overexpression affects neurite outgrowth, the addition of these factors would bias the experimental design, as these factors have been shown to improve axonal and neurite growth (12). In this sense, we evaluated neurite density and length when overexpressing Klotho with AVV9 vectors (AAV9-CMV-mKL and AAV9-CMV-sKL) or with recombinant sKL protein.

AAV9-CMV-sKL exhibited a significant increase in neurite density, roughly doubling the number of neurites compared to the untreated group (Fig. 8B). The overexpression of mKL also tended to increase neurite density. Nevertheless, the recombinant sKL protein only caused subtle changes, which is

interesting because it indicates a different behavior between the recombinant protein and AAV9 vector delivery. This might be due to the short half-life of the recombinant protein in culture (75), since it was only added in culture at the start of the experiment and not maintained over the following DIV. In contrast, although AAVs require time to express the transgene, sustained overexpression within neurons likely supports ongoing neurite growth. Regarding the length of the longest neurites, there were no significant differences between treatments (Fig. 8C). To support these manual analyses, we measured neurite intersections from the DRG explant with AAV-sKL treatment, as the difference in neurite density was statistically significant. As expected, we measured more neurite intersections near the DRG explant (Fig. 8D). Conversely, interactions at greater distances from the DRG explant were similar across treatments, reinforcing that there are no significant differences in the neurite length in the cultures upon sKL overexpression.

In summary, AAV9-mediated sKL overexpression promotes sensory neuritogenesis in rat DRG organotypic cultures. Organotypic cultures are useful for screening treatments before moving to *in vivo* models, thus contributing to the 3Rs principles, and here they provide the foundation for proposing the following *in vivo* experiments. Future studies will include recombinant sKL protein and the AAV9-CMV-mKL groups in the Neurite-J analysis. Subsequent studies could also include organotypic spinal cord cultures to study motor neurite growth or continue with DRG organotypic cultures while studying sustained addition of recombinant sKL protein.

Klotho enhances axonal regeneration and remyelination after sciatic nerve section

Several studies acknowledge the potential of Klotho in promoting myelination. *In vitro*, Klotho has been reported to support the proliferation and maturation of oligodendrocytes through the activation of Akt and ERK1/2 (47,76). Moving to *in vivo* evidence, researchers have generated an induced demyelination model using cuprizone, which leads to oligodendrocyte death and demyelination. In this model, transgenic animals overexpressing Klotho showed a significant increase in myelinated axonal density compared to wild-type controls (48). In addition, Klotho might also induce neuroprotection through its antioxidant and anti-inflammatory actions.

In light of this evidence, we aimed to evaluate, for the first time to our knowledge, the regenerative and remyelination capacities of Klotho within the peripheral nervous system using a cut-and-paste sciatic nerve model in adult mice. For therapeutic purposes, the viral vectors scAAV9-CMV-sKL and scAAV9-CMV-Null were administered intrathecally immediately after the injury. This type of injury was selected based on previous experience working with the adult sciatic nerve crush model, in which regeneration is highly effective and treatment differences are often subtle and difficult to detect. While the adult crush model causes minimal death of sensory neurons and motoneurons (73), this sciatic nerve section model, combined with fibrin glue, is more severe, but allows for partial nerve regeneration. sKL was chosen for overexpression via gene therapy based on the previous findings in organotypic DRG cultures. Moreover, mineral metabolism has been shown to be negatively affected by elevated serum pKL (proteolyzed mKL) levels (77). Furthermore, sKL has systemic hormonal effects, making it an optimal candidate for therapeutic overexpression.

The tibial nerve, a branch of the sciatic nerve, is commonly used for its large diameter and predominance of fast-conducting type A fibers (78), facilitating studies of regeneration after PNI. Overexpression of sKL led to a significant increase in axonal density, axonal diameter, and myelin

thickness (Fig. 10B, 10C, 10D, 10E, and 10F). These changes correlated with a g-ratio approaching the optimal value in mice for proper conduction velocity (Fig. 10G). This suggests that, following sciatic nerve cut-and-paste, intrathecal administration of scAAV9-CMV-sKL enhances axonal regeneration and remyelination in the tibial nerve after WD. These findings are further supported by improvements observed in electrophysiological functional tests performed in these animals.

However, one of the biggest limitations is the time-consuming nature of morphometric analyses. Given this technical complexity in histological analyses, automated tools have been developed (79,80), although not all are open-access and many are restricted to specific protocols. Therefore, manual measurements remain the gold-standard method in PNI analysis. The customized macro for Fiji was particularly useful, despite not eliminating the need for manual axon counting, it helped reduce the time needed to rename the interior and exterior of each axon, ensured measurements were paired, and automatically saved the ROIs for traceability of the results.

Selection of engineered AAV2 capsids with improved tropism for retinal neurons

This viral tropism study is the first step in selecting an AAV2 capsid with improved tropism toward retinal neurons, aiming to deliver sKL as a therapeutic transgene in the *Wfs*-deficient rat model with optic nerve atrophy and to several other models of retinal neurodegeneration, leading to blindness (31). The success of gene therapy for nerve regeneration depends not only on the key properties of the transgene, in this case Klotho, but also on the selection of the viral vector. Safety risks, immunogenicity, toxicity, genetic stability, packaging capacity, and high transduction efficiency in target cells are some characteristics of an ideal viral vector (54). Therefore, the AAV2.GL capsid has been engineered using a site-directed mutagenesis strategy with *in vivo* selection to increase transduction efficiency in retina from the natural AAV2 serotype (56). The main physical barrier for these vectors is crossing the inner limiting membrane (2). Additionally, several cell types can be targeted, such as photoreceptors, RGCs, and retinal epithelium.

We produced scAAV2-CMV-GFP, scAAV2.GL-CMV-GFP and scAAV2.GL-CAG-GFP, using GFP as a reporter. Vectors were administered intravitreally as a less invasive delivery route compared to the subretinal approach, thereby facilitating spread intra-cavity (53,56). Two ubiquitous promoters were tested, CMV and CAG (a hybrid of the CMV enhancer and the chicken β-actin promoter). The CMV promoter has a strong initial expression, although it has been shown to undergo transcriptional silencing via methylation over time (81), whereas the CAG promoter maintains sustained expression (82). Moreover, in a study comparing transduction in RGCs in the retina and optic nerve, with the CAG promoter, a higher transduction was detected, while transduction with CMV was lower (83). In this context, comparing AAV2-CMV with AAV2.GL-CMV showed a tendency towards more specific neuronal transduction with the modified capsid. This indicates that, even under the same promoter, AAV2.GL capsid modification can enhance neuronal transduction (Fig. 11B, 11C). As for the two promoters tested, we observed that the AAV2.GL vector with the CAG promoter showed the highest transduction and colocalization with neurons compared to the control. The AAV2.GL capsid under the control of the CMV promoter also showed increased transduction and neuronal colocalization compared to the control, although this difference was not statistically significant. This stronger transcription driven by CAG reflects that promoter selection further influences neuronal transduction efficiency.

Overall, the modified AAV2.GL capsid under the control of the CAG promoter exhibits enhanced tropism toward retinal neurons, indicating its potential in optic nerve injuries using sKL as a transgene. In an optic nerve transection model, Klotho has been related to the protection of RGCs by inhibiting apoptosis and reducing oxidative stress (84). Future studies could further investigate AAV2.GL-CAG expression through biodistribution studies, evaluate immunogenicity, and assess sKL efficacy in functional studies using the *Wfs*-deficient rat model. Additionally, neuron-specific promoters, such as the human synapsin promoter (hSyn), could be investigated to enhance targeted expression in retinal neurons.

CONCLUSIONS

1. α-Klotho mRNA expression is downregulated after sciatic nerve resection in hindlimb muscles (TA, GM, Sol, and EDL) and the spinal cord.
2. α-Klotho isoforms show temporal and tissue-dependent differential mRNA regulation after sciatic nerve crush.
3. Neurite outgrowth in rat DRG organotypic culture is promoted by AAV9-mediated sKL overexpression.
4. Axonal regeneration and remyelination are enhanced in the tibial nerve after sciatic nerve cut-and-paste with intrathecal administration of scAAV9-CMV-sKL.
5. The novel AAV2.GL capsid efficiently transduces retinal neurons via intravitreal administration, with the CAG promoter achieving higher expression than the CMV promoter.

BIBLIOGRAPHY

1. Ludwig PE, Reddy V, Varacallo MA. Neuroanatomy, Central Nervous System (CNS). In: StatPearls [Internet]. Treasure Island (FL): StatPearls Publishing; 2025 [cited 2025 Aug 11]. Available from: http://www.ncbi.nlm.nih.gov/books/NBK442010/

2. Herrera E, Agudo-Barriuso M, Murcia-Belmonte V. Cranial Pair II: The Optic Nerves. The Anatomical Record. 2019;302(3):428–45.

3. Allen NJ, Lyons DA. Glia as architects of central nervous system formation and function. Science. 2018 Oct 12;362(6411):181–5.

4. Liu Y, Shen X, Zhang Y, Zheng X, Cepeda C, Wang Y, et al. Interactions of glial cells with neuronal synapses, from astrocytes to microglia and oligodendrocyte lineage cells. Glia. 2023;71(6):1383–401.

5. Kirby ED, Glenn MJ, Sandstrom NJ, Williams CL. 1.5 The Peripheral Nervous System: PNS - Introduction to Behavioral Neuroscience | OpenStax [Internet]. OpenStax; 2024 [cited 2025 Aug 11]. Available from: https://openstax.org/books/introduction-behavioral-neuroscience/pages/1-5-the-peripheral-nervous-system-pns

6. Firmin L, Field P, Maier MA, Kraskov A, Kirkwood PA, Nakajima K, et al. Axon diameters and conduction velocities in the macaque pyramidal tract. Journal of Neurophysiology [Internet]. 2014 Sept 15 [cited 2025 Aug 13]; Available from: https://journals.physiology.org/doi/10.1152/jn.00720.2013

7. Magnéli M, Axenhus M. Epidemiology and regional variance of traumatic peripheral nerve injuries in Sweden: A 15-year observational study. PLoS One. 2024 Oct 9;19(10):e0310988.

8. Murphy RNA, de Schoulepnikoff C, Chen JHC, Columb MO, Bedford J, Wong JK, et al. The incidence and management of peripheral nerve injury in England (2005-2020). J Plast Reconstr Aesthet Surg. 2023 May;80:75–85.

9. Noble J, Munro CA, Prasad VSSV, Midha R. Analysis of Upper and Lower Extremity Peripheral Nerve Injuries in a Population of Patients with Multiple Injuries. Journal of Trauma and Acute Care Surgery. 1998 July;45(1):116.

10. Seddon HJ. Three types of nerve injury. Brain. 1943 Dec 1;66(4):237–88.

11. Sunderland S. A classification of peripheral nerve injuries producing loss of funtion. Brain. 1951 Dec 1;74(4):491–516.

12. Alvites R, Rita Caseiro A, Santos Pedrosa S, Vieira Branquinho M, Ronchi G, Geuna S, et al. Peripheral nerve injury and axonotmesis: State of the art and recent advances. Spurkland A, editor. Cogent Medicine. 2018 Jan;5(1):1466404.

13. Mackinnon SE, Dellon AL. Diagnosis of nerve injury. In: Surgery of the peripheral nerve. New York: Thieme; 1988. p. 74–9.

14. Pellegatta M, Taveggia C. The Complex Work of Proteases and Secretases in Wallerian Degeneration: Beyond Neuregulin-1. Front Cell Neurosci [Internet]. 2019 Mar 20 [cited 2025 Aug 13];13. Available from: https://www.frontiersin.org/journals/cellular-neuroscience/articles/10.3389/fncel.2019.00093/full

15. Lopes B, Sousa P, Alvites R, Branquinho M, Sousa AC, Mendonça C, et al. Peripheral Nerve Injury Treatments and Advances: One Health Perspective. International Journal of Molecular Sciences. 2022 Jan;23(2):918.

16. Kılıçarslan O, Yılmaz Çebi A, Batu Oto B, Yıldırım R. Demographics and etiologic characteristics of non-glaucomatous optic atrophy: a single-center cross-sectional study from Turkey. Int Ophthalmol. 2022 Nov 1;42(11):3521–9.

17. Shrestha P, Sitaula S, Sharma AK, Joshi P. Clinical Assessment and Etiological Evaluation of Optic Nerve Atrophy. Nep J Oph. 2021 Jan 1;13(1):73–81.

18. Kang EYC, Liu PK, Wen YT, Quinn PMJ, Levi SR, Wang NK, et al. Role of Oxidative Stress in Ocular Diseases Associated with Retinal Ganglion Cells Degeneration. Antioxidants. 2021 Dec;10(12):1948.

19. Buonfiglio F, Böhm EW, Pfeiffer N, Gericke A. Oxidative Stress: A Suitable Therapeutic Target for Optic Nerve Diseases? Antioxidants. 2023 July;12(7):1465.

20. Maresca A, Carelli V. Molecular Mechanisms behind Inherited Neurodegeneration of the Optic Nerve. Biomolecules. 2021 Apr;11(4):496.

21. Carelli V, Ross-Cisneros FN, Sadun AA. Mitochondrial dysfunction as a cause of optic neuropathies. Progress in Retinal and Eye Research. 2004 Jan 1;23(1):53–89.

22. Coleman-Belin J, Harris A, Chen B, Zhou J, Ciulla T, Verticchio A, et al. Aging Effects on Optic Nerve Neurodegeneration. International Journal of Molecular Sciences. 2023 Jan;24(3):2573.

23. Allodi I, Udina E, Navarro X. Specificity of peripheral nerve regeneration: Interactions at the axon level. Progress in Neurobiology. 2012 July 1;98(1):16–37.

24. Scheib J, Höke A. Advances in peripheral nerve regeneration. Nat Rev Neurol. 2013 Dec;9(12):668–76.

25. Akram R, Anwar H, Javed MS, Rasul A, Imran A, Malik SA, et al. Axonal Regeneration: Underlying Molecular Mechanisms and Potential Therapeutic Targets. Biomedicines. 2022 Dec;10(12):3186.

26. Klimovich P, Rubina K, Sysoeva V, Semina E. New Frontiers in Peripheral Nerve Regeneration: Concerns and Remedies. International Journal of Molecular Sciences. 2021 Jan;22(24):13380.

27. Richardson PM, McGuinness UM, Aguayo AJ. Axons from CNS neurones regenerate into PNS grafts. Nature. 1980 Mar;284(5753):264–5.

28. Li A, Pereira C, Hill EE, Vukcevic O, Wang A. In Vitro, In Vivo and Ex Vivo Models for Peripheral Nerve Injury and Regeneration. Curr Neuropharmacol. 2022 Feb 17;20(2):344–61.

29. Geuna S. The sciatic nerve injury model in pre-clinical research. Journal of Neuroscience Methods. 2015 Mar 30;243:39–46.

30. Akhter ET, Rotterman TM, English AW, Alvarez FJ. Sciatic Nerve Cut and Repair Using Fibrin Glue in Adult Mice. Bio-protocol [Internet]. 2019 Sept 20 [cited 2025 Aug 14];9(18). Available from: https://bio-protocol.org/en/bpdetail?id=3363&type=0

31. Plaas M, Seppa K, Reimets R, Jagomäe T, Toots M, Koppel T, et al. Wfs1- deficient rats develop primary symptoms of Wolfram syndrome: insulin-dependent diabetes, optic nerve atrophy and medullary degeneration. Sci Rep. 2017 Aug 31;7(1):10220.

32. Kuro-o M. Klotho and the Aging Process. Korean J Intern Med. 2011 June 1;26(2):113–22.

33. Kuro-o M, Matsumura Y, Aizawa H, Kawaguchi H, Suga T, Utsugi T, et al. Mutation of the mouse klotho gene leads to a syndrome resembling ageing. Nature. 1997 Nov;390(6655):45–51.

34. Massó A, Sánchez A, Gimenez-Llort L, Lizcano JM, Cañete M, García B, et al. Secreted and Transmembrane αKlotho Isoforms Have Different Spatio-Temporal Profiles in the Brain during Aging and Alzheimer's Disease Progression. PLOS ONE. 2015 Nov 24;10(11):e0143623.

35. Prud'homme GJ, Kurt M, Wang Q. Pathobiology of the Klotho Antiaging Protein and Therapeutic Considerations. Front Aging [Internet]. 2022 July 12 [cited 2025 May 31];3. Available from: https://www.frontiersin.org/journals/aging/articles/10.3389/fragi.2022.931331/full

36. Kurosu H, Yamamoto M, Clark JD, Pastor JV, Nandi A, Gurnani P, et al. Suppression of aging in mice by the hormone Klotho. Science. 2005 Sept 16;309(5742):1829–33.

37. Castner SA, Gupta S, Wang D, Moreno AJ, Park C, Chen C, et al. Longevity factor klotho enhances cognition in aged nonhuman primates. Nat Aging. 2023 Aug;3(8):931–7.

38. Welc SS, Wehling-Henricks M, Kuro-o M, Thomas KA, Tidball JG. Modulation of Klotho expression in injured muscle perturbs Wnt signalling and influences the rate of muscle growth. Experimental Physiology. 2020;105(1):132–47.

39. Roig-Soriano J, Sánchez-de-Diego C, Esandi-Jauregui J, Verdés S, Abraham CR, Bosch A, et al. Differential toxicity profile of secreted and processed α-Klotho expression over mineral metabolism and bone microstructure. Sci Rep. 2023 Mar 14;13(1):4211.

40. Chen G, Liu Y, Goetz R, Fu L, Jayaraman S, Hu MC, et al. α-Klotho is a non-enzymatic molecular scaffold for FGF23 hormone signalling. Nature. 2018 Jan;553(7689):461–6.

41. Dalton GD, Xie J, An SW, Huang CL. New Insights into the Mechanism of Action of Soluble Klotho. Front Endocrinol [Internet]. 2017 Nov 17 [cited 2025 Aug 16];8. Available from: https://www.frontiersin.org/journals/endocrinology/articles/10.3389/fendo.2017.00323/full

42. Lim K, Groen A, Molostvov G, Lu T, Lilley KS, Snead D, et al. α-Klotho Expression in Human Tissues. J Clin Endocrinol Metab. 2015 Oct 1;100(10):E1308–18.

43. Zhang Y, Wang L, Wu Z, Yu X, Du X, Li X. The Expressions of Klotho Family Genes in Human Ocular Tissues and in Anterior Lens Capsules of Age-Related Cataract. Current Eye Research. 2017 June 3;42(6):871–5.

44. King GD, Rosene DL, Abraham CR. Promoter methylation and age-related downregulation of Klotho in rhesus monkey. Age (Dordr). 2012 Dec;34(6):1405–19.

45. Fung TY, Iyaswamy A, Sreenivasmurthy SG, Krishnamoorthi S, Guan XJ, Zhu Z, et al. Klotho an Autophagy Stimulator as a Potential Therapeutic Target for Alzheimer's Disease: A Review. Biomedicines. 2022 Mar;10(3):705.

46. Jiang Y, Wen X, Jian X, Chen Q, Li Y. Klotho attenuates epithelial-mesenchymal transition of retinal pigment epithelial cells in subretinal fibrosis by suppressing the ERK1/2 and Wnt/β-catenin signaling pathways. International Journal of Molecular Medicine. 2025 Mar 1;55(3):1–14.

47. Chen CD, Li H, Liang J, Hixson K, Zeldich E, Abraham CR. The Anti-Aging and Tumor Suppressor Protein Klotho Enhances Differentiation of a Human Oligodendrocytic Hybrid Cell Line. J Mol Neurosci. 2015 Jan;55(1):76–90.

48. Zeldich E, Chen CD, Avila R, Medicetty S, Abraham CR. The Anti-Aging Protein Klotho Enhances Remyelination Following Cuprizone-Induced Demyelination. J Mol Neurosci. 2015 Oct 1;57(2):185–96.

49. Sahu A, Mamiya H, Shinde SN, Cheikhi A, Winter LL, Vo NV, et al. Age-related declines in α-Klotho drive progenitor cell mitochondrial dysfunction and impaired muscle regeneration. Nat Commun. 2018 Nov 19;9(1):4859.

50. Bean LA, Thomas C, Villa JF, Fitt AJ, Javier AJS, Agrawal A, et al. Klotho deficiency promotes skeletal muscle weakness and is associated with impaired motor unit connectivity. bioRxiv. 2025 June 17;2025.06.11.659129.

51. Avin KG, Coen PM, Huang W, Stolz DB, Sowa GA, Dubé JJ, et al. Skeletal muscle as a regulator of the longevity protein, Klotho. Front Physiol [Internet]. 2014 June 17 [cited 2025 Aug 16];5. Available from: https://www.frontiersin.org/journals/physiology/articles/10.3389/fphys.2014.00189/full

52. Bulcha JT, Wang Y, Ma H, Tai PWL, Gao G. Viral vector platforms within the gene therapy landscape. Sig Transduct Target Ther. 2021 Feb 8;6(1):53.

53. Wang JH, Gessler DJ, Zhan W, Gallagher TL, Gao G. Adeno-associated virus as a delivery vector for gene therapy of human diseases. Sig Transduct Target Ther. 2024 Apr 3;9(1):1–33.

54. Wang D, Tai PWL, Gao G. Adeno-associated virus vector as a platform for gene therapy delivery. Nat Rev Drug Discov. 2019 May;18(5):358–78.

55. Nisanov AM, Rivera de Jesús JA, Schaffer DV. Advances in AAV capsid engineering: Integrating rational design, directed evolution and machine learning. Molecular Therapy. 2025 May 7;33(5):1937–45.

56. Pavlou M, Schön C, Occelli LM, Rossi A, Meumann N, Boyd RF, et al. Novel AAV capsids for intravitreal gene therapy of photoreceptor disorders. EMBO Molecular Medicine. 2021 Apr 9;13(4):e13392.

57. Piedra J, Ontiveros M, Miravet S, Penalva C, Monfar M, Chillon M. Development of a Rapid, Robust, and Universal PicoGreen-Based Method to Titer Adeno-Associated Vectors. Human Gene Therapy Methods. 2015 Feb;26(1):35–42.

58. Bauder AR, Ferguson TA. Reproducible Mouse Sciatic Nerve Crush and Subsequent Assessment of Regeneration by Whole Mount Muscle Analysis. JoVE. 2012 Feb 22;(60):3606.

59. Torres-Espín A, Santos D, González-Pérez F, del Valle J, Navarro X. Neurite-J: An Image-J plug-in for axonal growth analysis in organotypic cultures. Journal of Neuroscience Methods. 2014 Oct 30;236:26–39.

60. Pfaffl MW. A new mathematical model for relative quantification in real-time RT-PCR. Nucleic Acids Research. 2001 May 1;29(9):45e–45.

61. Rigoard P. The Sciatic Nerve. In: Rigoard P, editor. Atlas of Anatomy of the Peripheral Nerves : The Nerves of the Limbs – Student Edition [Internet]. Cham: Springer International Publishing; 2017 [cited 2025 Aug 25]. p. 224–43. Available from: https://doi.org/10.1007/978-3-319-43089-8_15

62. Bailey RM, Rozenberg A, Gray SJ. Comparison of high-dose intracisterna magna and lumbar puncture intrathecal delivery of AAV9 in mice to treat neuropathies. Brain Research. 2020 July 15;1739:146832.

63. Homs J, Pagès G, Ariza L, Casas C, Chillón M, Navarro X, et al. Intrathecal administration of IGF-I by AAVrh10 improves sensory and motor deficits in a mouse model of diabetic neuropathy. Molecular Therapy Methods & Clinical Development [Internet]. 2014 Jan 1 [cited 2025 Sept 1];1. Available from: https://www.cell.com/molecular-therapy-family/methods/abstract/S2329-0501(16)30072-9

64. Rushton WAH. A theory of the effects of fibre size in medullated nerve. J Physiol. 1951 Sept 28;115(1):101–22.

65. Sahu A, Clemens ZJ, Shinde SN, Sivakumar S, Pius A, Bhatia A, et al. Regulation of aged skeletal muscle regeneration by circulating extracellular vesicles. Nat Aging. 2021 Dec;1(12):1148–61.

66. Bloemberg D, Quadrilatero J. Rapid Determination of Myosin Heavy Chain Expression in Rat, Mouse, and Human Skeletal Muscle Using Multicolor Immunofluorescence Analysis. PLOS ONE. 2012 Apr 18;7(4):e35273.

67. Talbot J, Maves L. Skeletal muscle fiber type: using insights from muscle developmental biology to dissect targets for susceptibility and resistance to muscle disease. WIREs Developmental Biology. 2016;5(4):518–34.

68. Bastien D, Lacroix S. Cytokine pathways regulating glial and leukocyte function after spinal cord and peripheral nerve injury. Experimental Neurology. 2014 Aug 1;258:62–77.

69. Pottorf TS, Rotterman TM, McCallum WM, Haley-Johnson ZA, Alvarez FJ. The Role of Microglia in Neuroinflammation of the Spinal Cord after Peripheral Nerve Injury. Cells. 2022 Jan;11(13):2083.

70. Cuevas-Diaz Duran R, Li Y, Garza Carbajal A, You Y, Dessauer CW, Wu J, et al. Major Differences in Transcriptional Alterations in Dorsal Root Ganglia Between Spinal Cord Injury and Peripheral Neuropathic Pain Models. Journal of Neurotrauma. 2023 May;40(9–10):883–900.

71. Hu G, Huang K, Hu Y, Du G, Xue Z, Zhu X, et al. Single-cell RNA-seq reveals distinct injury responses in different types of DRG sensory neurons. Sci Rep. 2016 Aug 25;6(1):31851.

72. Liu Y, Wang H. Peripheral nerve injury induced changes in the spinal cord and strategies to counteract/enhance the changes to promote nerve regeneration. Neural Regen Res. 2019 Sept 24;15(2):189–98.

73. Kemp SWP, Chiang CD, Liu EH, Wood MD, Willand MP, Gordon T, et al. Characterization of Neuronal Death and Functional Deficits following Nerve Injury during the Early Postnatal Developmental Period in Rats. Dev Neurosci. 2015 Jan 13;37(1):66–77.

74. Bozkurt A, Brook GA, Moellers S, Lassner F, Sellhaus B, Weis J, et al. In Vitro Assessment of Axonal Growth Using Dorsal Root Ganglia Explants in a Novel Three-Dimensional Collagen Matrix. Tissue Engineering. 2007 Dec;13(12):2971–9.

75. Zhong X, Jagarlapudi S, Weng Y, Ly M, Rouse JC, McClure K, et al. Structure-function relationships of the soluble form of the antiaging protein Klotho have therapeutic implications for managing kidney disease. J Biol Chem. 2020 Mar 6;295(10):3115–33.

76. Chen CD, Sloane JA, Li H, Aytan N, Giannaris EL, Zeldich E, et al. The Antiaging Protein Klotho Enhances Oligodendrocyte Maturation and Myelination of the CNS. J Neurosci. 2013 Jan 30;33(5):1927–39.

77. Roig-Soriano J, Sánchez-de-Diego C, Esandi-Jauregui J, Verdés S, Abraham CR, Bosch A, et al. Differential toxicity profile of secreted and processed α-Klotho expression over mineral metabolism and bone microstructure. Sci Rep. 2023 Mar 14;13(1):4211.

78. Whitwam JG. Classification of peripheral nerve fibres. Anaesthesia. 1976;31(4):494–503.

79. Daeschler SC, Bourget MH, Derakhshan D, Sharma V, Asenov SI, Gordon T, et al. Rapid, automated nerve histomorphometry through open-source artificial intelligence. Sci Rep. 2022 Apr 8;12(1):5975.

80. Orfahli LM, Rezaei M, Figueroa BA, Crawford AV, Annunziata MJ, Rao M, et al. Histomorphometry in Peripheral Nerve Regeneration: Comparison of Different Axon Counting Methods. Journal of Surgical Research. 2021 Dec 1;268:354–62.

81. Gray SJ, Foti SB, Schwartz JW, Bachaboina L, Taylor-Blake B, Coleman J, et al. Optimizing Promoters for Recombinant Adeno-Associated Virus-Mediated Gene Expression in the Peripheral and Central Nervous System Using Self-Complementary Vectors. Human Gene Therapy. 2011 Sept;22(9):1143–53.

82. Klein RL, Hamby ME, Gong Y, Hirko AC, Wang S, Hughes JA, et al. Dose and Promoter Effects of Adeno-Associated Viral Vector for Green Fluorescent Protein Expression in the Rat Brain. Experimental Neurology. 2002 July 1;176(1):66–74.

83. Nieuwenhuis B, Laperrousaz E, Tribble JR, Verhaagen J, Fawcett JW, Martin KR, et al. Improving adeno-associated viral (AAV) vector-mediated transgene expression in retinal ganglion cells: comparison of five promoters. Gene Ther. 2023 June;30(6):503–19.

84. Yamamoto K, Sato K, Yukita M, Yasuda M, Omodaka K, Ryu M, et al. The neuroprotective effect of latanoprost acts via klotho-mediated suppression of calpain activation after optic nerve transection. Journal of Neurochemistry. 2017;140(3):495–508.